ANL-78-79

ANL-78-79

MATERIALS TECHNOLOGY FOR COAL-CONVERSION PROCESSES

Fourteenth Quarterly Report, April—June 1978

U of C-AUA-USDOE

ARGONNE NATIONAL LABORATORY, ARGONNE, ILLINOIS

Prepared for the Office of Fossil Energy,
U. S. DEPARTMENT OF ENERGY
under Contract W-31-109-Eng-38

DISCLAIMER

Printed in the United States of America
Available from
National Technical Information Service
U. S. Department of Commerce
5285 Port Royal Road
Springfield, Virginia 22161
Price: Printed Copy $5.25; Microfiche $3.00

Distribution Category:
Coal Conversion and Utilization—
Coal Gasification (UC-90c)

ANL-78-79

ARGONNE NATIONAL LABORATORY
9700 South Cass Avenue
Argonne, Illinois 60439

0442 8000

MATERIALS TECHNOLOGY FOR COAL-CONVERSION PROCESSES

Fourteenth Quarterly Report,
April—June 1978

W. A. Ellingson
Project Leader

Materials Science Division

Previous reports in this series

ANL-76-7	July—September 1975
ANL-76-22	October—December 1975
ANL-76-60	January—March 1976
ANL-76-111	April—June 1976
ANL-76-125	July—September 1976
ANL-77-5	October—December 1976
ANL-77-41	January—March 1977
ANL-77-62	April—June 1977
ANL-78-6	July—December 1977
ANL-78-54	January—March 1978

THIS PAGE

WAS INTENTIONALLY

LEFT BLANK

LIST OF FIGURES

LIST OF FIGURES (Contd.)

LIST OF TABLES

MATERIALS TECHNOLOGY FOR COAL-CONVERSION PROCESSES: FOURTEENTH QUARTERLY REPORT, APRIL-JUNE 1978

HIGHLIGHTS

Task A -- Evaluation of Ceramic Refractories for Slagging Gasifiers *(C.R. Kennedy, D.J. Jones, and R.J. Fousek)*

Optical and SEM examinations of alumina, alumina-chrome, magnesia-chrome, and chrome-spinel refractories exposed to acid slags in some previous test runs show that spinel reaction products form at the slag-refractory interface.

Task C -- Application and Development of Nondestructive Evaluation Methods for Coal-conversion Processes *(W.A. Ellingson, K.J. Reimann, W.J. Shack, and C.A. Youngdahl)*

Comparison of the surface crack patterns of two high-alumina panels fired at different heating rates reveals few characteristic differences. This finding agrees qualitatively with the acoustic-emission data, which suggest that cracking occurs at different times in the two panels but that the cracking patterns are similar.

To determine the effect of surface roughness on wall-erosion measurements, ultrasonic wave-scattering data acquisition and processing equipment were assembled. The spectral content of waves reflected off the front and back of periodically roughened surfaces were compared. Scattering off the back surface is clearly much more complex than scattering off the front surface.

Ultrasonically measured erosive-wear data on the HYGAS cyclone have been obtained after more than 3000 h of operation; the linear rate is nearly the same as that observed in past examinations.

In-situ erosive-wear data were obtained on BI-GAS and Synthane plant components. Study is in progress to establish more uniform field-welds.

A field test program for acoustic valve leakage detection systems for use at the Morgantown Energy Technology Center was planned. Arrangements were made at Morgantown to install two acoustic valve leak detection systems for field data acquisition. The acoustic systems installed have been developed by Argonne and the U.S. Naval Ship Research and Development Center.

Task D -- Corrosion Behavior of Materials in Coal-conversion Processes *(K. Natesan)*

Uniaxial tensile data were generated for Incoloy 800, Type 310 stainless steel, U.S. Steel Alloy 18-18-2, and Inconel 671 after 3.6-Ms exposures to multicomponent gas mixtures that simulate a coal-gasification environment. The preexposure of the materials to complex gas mixtures resulted in a decrease in ultimate tensile strength with only minimal changes in the uniform strain over the range of $\sim$ 4 to 13%.

Task E -- Erosion Behavior of Materials in Coal-conversion Processes *(J.Y. Park and W.J. Shack)*

Installation work continued on the high-temperature erosion apparatus. Particle velocities and trajectories have been obtained through frame-by-frame analysis of high-speed motion pictures. Benchmark room-temperature tests have been carried out on structural alloys.

Task F -- Component Performance and Failure Analysis *(S. Danyluk, G.M. Dragel, L. Pahis, J.Y. Park, M. Nimalendran, S. Greenberg, J.C. Florek, J. Wang, S. Mihailovich, R.H. Lee)*

Failed components from the HYGAS Ash Agglomerating Gasifer (dipleg, thermowell and pressure tap) and the Synthane pilot plant (CO_2-compressor unloading fingers, eighth-floor oxygen line, steam heat up line, raw-gas scrubber, char-transfer line, oxygen line #1203 and oxygen line #1381) were examined during the current quarter.

MATERIALS TECHNOLOGY FOR COAL-CONVERSION PROCESSES: FOURTEENTH QUARTERLY REPORT, APRIL-JUNE 1978

ABSTRACT

This broad-base materials engineering program, begun in 1974, includes studies on ceramic (refractory) and metallic materials presently being used or intended for use in coal-conversion processes. The program entails studies of erosive wear, nondestructive testing, corrosion, refractory degradation, and failure analysis. Appropriate laboratory and field experiments are integrated such that the results have impact on present pilot-plant and proposed demonstration-plant designs. This quarterly report, for the period April-June 1978, presents the technical accomplishments of the program.

INTRODUCTION

The economical conversion of coal into clean and usable fuels will be advanced through the use of durable materials systems. The technical information base required for materials selection in plant design for the operating environments of various coal-conversion processes is extremely limited. Hence, reliable selection and lifetime prediction methods of materials under these conditions are not available. This project is designed to provide part of the materials information necessary for successful operation of coal-conversion systems. The present report is the fourteenth quarterly progress report submitted by ANL to the Division of System Engineering, Office of Fossil Energy under project Number 7106, "Materials Technology for Coal Conversion Processes".

The project includes six tasks: (A) evaluation of commercial refractories exposed to coal slag under conditions typical of those encountered in slagging gasification processes; (B) evaluation of erosion/corrosion-resistant coatings when exposed to prototype operating environments; (C) development, evaluation, and application of nondestructive evaluation methods applicable to coal-conversion systems; (D) evaluation of the corrosion behavior of commercial alloys; (E) development of analytical models to predict the erosive-wear behavior of materials used in coal-conversion plants; and (F) analysis of failed coal-conversion plant components.

Task A -- Evaluation of Ceramic Refractories for Slagging Gasifiers
(C.R. Kennedy, D.J. Jones, and R.J. Fousek)

Test run 9 in the slag-abrasion/corrosion test facility has been completed and the results are presently being compiled and analyzed. Included in this test were a chrome-spinel (number 22), a chrome-alumina (number 38), an alumina-silica (number 14), and three silicon carbide (numbers 37, 91 and 93) refractories. A complete documentation of the corrosion, temperature, thermal profiles in the bricks, partial pressure of oxygen, and slag composition as functions of time will be presented in the next quarterly report.

Much of the effort this quarter has been devoted to determining the mechanism of attack in selected refractories exposed in previous tests. To date, several magnesia-chrome and alumina-chrome refractories from test runs 5-7 have been examined. Figures 1a-h illustrate a typical reaction that occurred between an acid slag and a water-cooled magnesia-chrome refractory (number 29) during test run 5. Figure 1a was taken using reflected light, whereas Figs. 1b-h are of the same area in the sample but were produced with a scanning-electron microscope. Note that Fig. 1a is a mirror image of Figs. 1b-h. Visible in the upper part of Figs. 1a and 1b is a Mg-rich grain containing some Cr, Fe, and Al (in the form of spheroidal precipitates of spinel) which, along with Cr-Al-Fe-rich grains, was typical of the unaltered microstructure. The centers of Figs. 1a and 1b show a lacework structure of complex $(Mg,Fe)O\cdot(Cr,Al,Fe)_2O_3$ spinel, which recrystallized within the Ca-Si-rich slag (primarily melilite, $2CaO\cdot Al_2O_3\cdot SiO_2$-$2CaO\cdot MgO\cdot 2SiO_2$) after the bulk of the magnesia in the grain had been preferentially dissolved to form diopside ($CaO\cdot MgO\cdot 2SiO_2$).

Figures 2a-h detail the reaction that occurred when a water-cooled alumina-chrome refractory (number 852) was exposed to an acid slag in test run 7. The virgin refractory was composed mainly of large alumina grains in a Cr_2O_3-rich matrix. Solid solution of the Cr_2O_3 matrix around the rims of the Al_2O_3 grains was evident in both the virgin and exposed samples (see upper right side of Figs. 2c and 2d). On the lower left of Fig. 2a is the Ca- and Si-rich slag. Adjacent to this slag layer is a refractory-slag reaction layer consisting of a complex $(Mg,Fe)O\cdot(Cr,Al,Fe)_2O_3$ spinel similar in composition to that formed in the magnesia-chrome refractories. However, the structures of these spinel reaction products differ significantly. Herein lies the probable explanation for the superior performance of the water-cooled alumina-chrome refractories in comparison with the water-cooled magnesia-chrome refractories. In the magnesia-chrome refractories, the excess magnesia was preferentially dissolved by the slag, leaving a recrystallized spinel with an open lacework structure. However, the alumina-chrome refractories contain no magnesia initially, so magnesia (and iron) from the slag react with the refractory to form a solid spinel layer at the slag-refractory interface, which offers a greater degree of protection from further corrosion than does an open structure.

The composition of this spinel layer is also important. The corrosion resistance of the alumina-chrome and chrome-alumina refractories increased as the chromia content increased. A similar trend (although the range of chromia content was small) was noted in the magnesia-chrome refractories. Since exact phase diagrams for these particular complex systems are not available, supporting evidence must be drawn from studies of similar systems. Examination of a pseudobinary system,[1] which represents the change in liquidus temperature of the sextuple-point compositions in the $CaO-MgO-Al_2O_3-Cr_2O_3-SiO_2$ system [involving chrome ($MgO \cdot Cr_2O_3$), periclase, monticellite, and forsterite] in terms of the $MgO \cdot Al_2O_3$:$MgO \cdot Cr_2O_3$ weight-percent ratio, shows that the liquidus temperature rises rapidly from 1420 to 1500°C as the percentage of $MgO \cdot Cr_2O_3$ increases to 100%. This indicates that $MgO \cdot Cr_2O_3$ spinels are higher melting than $MgO \cdot Al_2O_3$ spinels in the presence of complex systems containing CaO and SiO_2. Additional evidence is presented which shows that the $MgO \cdot Al_2O_3$ portion of chrome crystals in a silicate bonded magnesia-chrome refractory is preferentially dissolved in the silicate matrix.

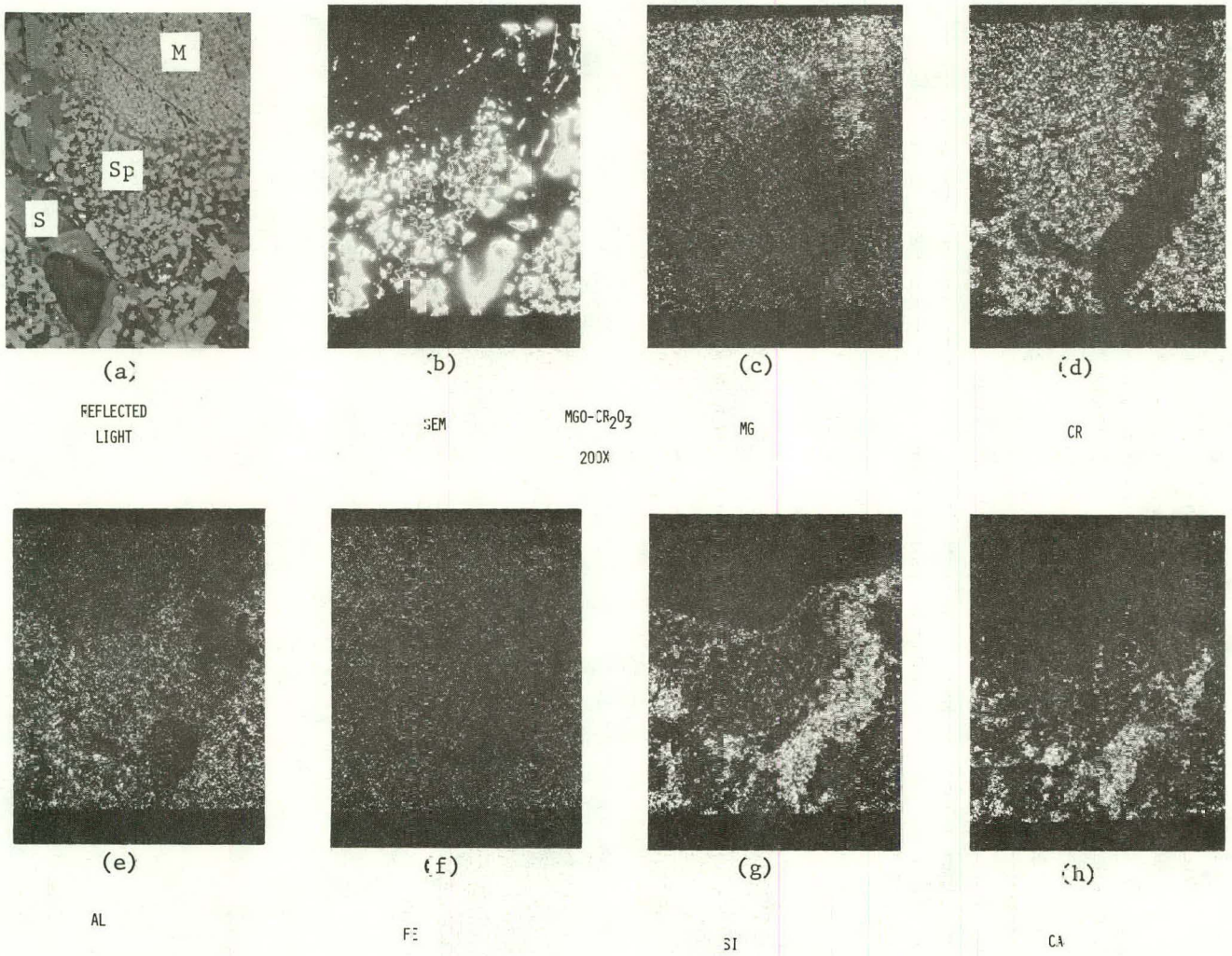

Fig. 1. Slag-Refractory Interface of a Magnesia-Chrome Refractory (Number 29) Exposed to an Acid Slag (B/A = 0.6). (a) In reflected light, (b) SEM, (c) Mg scan, (d) Cr scan, (e) Al scan, (f) Fe scan, (g) Si scan, and (h) Ca scan. Note that (a) is the mirror image of (b)-(h). M = original magnesia grain with spinel precipitates; Sp = recrystallized spinel; S = slag. Magnification, 200X. Neg. No. MSD-65385.

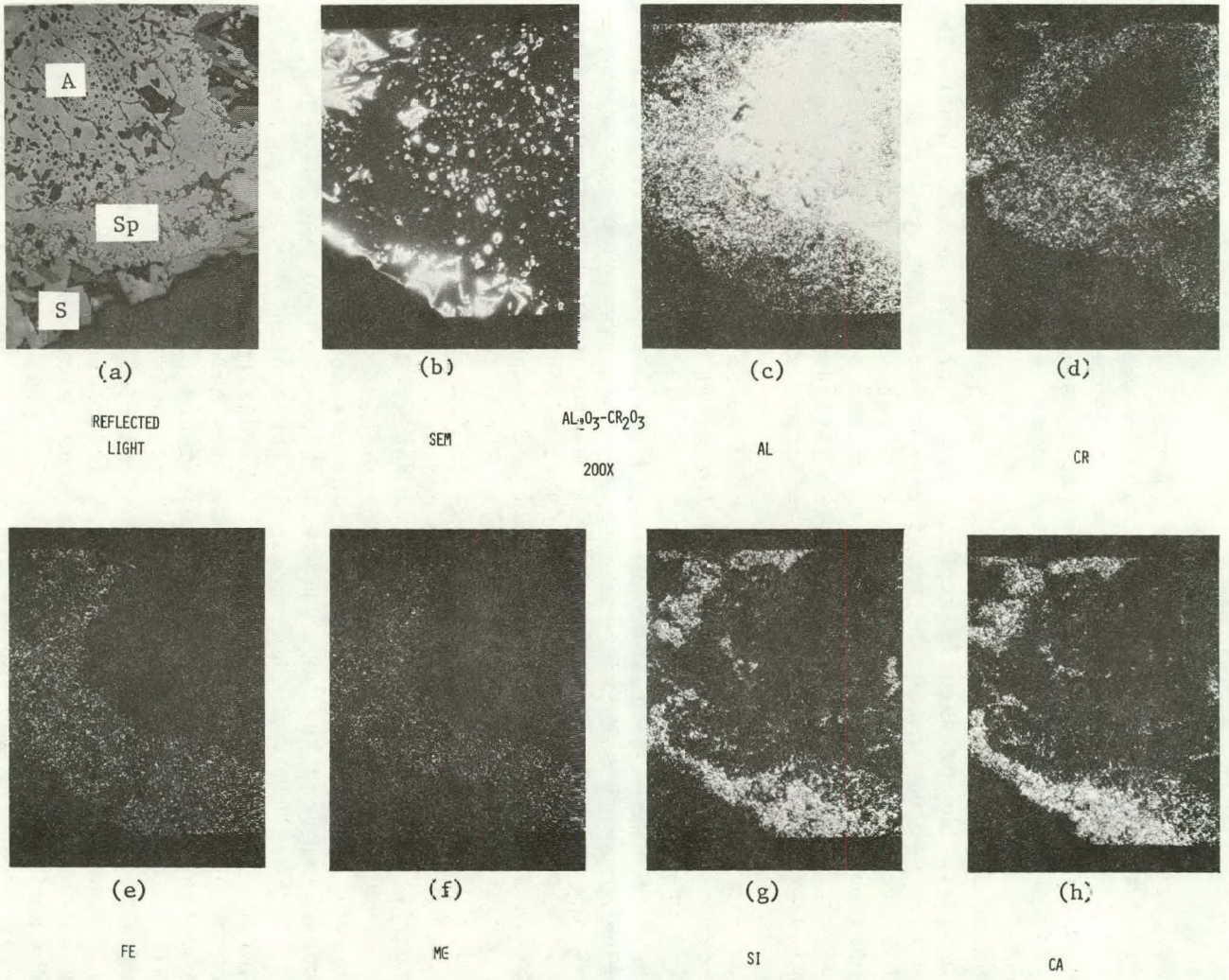

Fig. 2. Slag-Refractory Interface of an Alumina-Chrome Refractory (Number 852) Exposed to an Acid Slag (B/A = 0.7). (a) In reflected light, (b) SEM, (c) Al scan, (d) Cr scan, (e) Fe scan, (f) Mg scan, (g) Si scan, and (h) Ca scan. Note that (a) is the mirror image of (b)-(h). A = alumina grains; Sp = spinel; S = slag. Magnification, 200X. Neg. No. MSD-65384

Task C -- Application and Development of Nondestructive Evaluation Methods for Coal-conversion Processes *(W.A. Ellingson, K.J. Reimann, W.J. Shack, and C.A. Youngdahl)*

1. Erosive-wear Detection and Monitoring

a. Metallic Transfer Lines

(1) Ultrasonic Studies - Pilot Plants. The experimental ultrasonic monitoring of erosion in metallic components of coal-conversion pilot plants has continued this quarter, and the development of ultrasonic systems for on-line erosion detection has progressed. Posttest data have been obtained from the Mark II instrumented elbow[2] which was removed from the main coal-feed line of the Synthane Pilot Plant. Stellite wear data from the HYGAS effluent cyclone[2] after more than 3000 h of operation have been used to update the previously reported plot[3] of wear against operating time. Connecting cables of the ANL erosive-wear detection system[2] at the Bi-Gas Pilot Plant, which were damaged after a burner rupture in February, have been repaired. Efforts to improve the method of field attachment of ultrasonic waveguides to metallic lines have included evaluation of a set of test samples prepared by a commercial welding firm.

The Mark II instrumented elbow, used to convey Illinois #6 coal into the process system of the Synthane Pilot Plant from August, 1977, to February 1978, was returned to ANL and examined. Because some additional coal throughput occurred after the final in-situ ultrasonic survey of erosion on January 28, the waveguide sites were surveyed once again. Somewhat less erosive wear was indicated by these laboratory determinations than was evident from the field measurements described in the previous quarterly report.[2] However, the total wear was small and comparable to the error band of the field measurements (± 0.13 mm). The 0.3-m-radius, 90°-bend elbow, formed of 1-in. schedule 80 Type 304 stainless steel pipe, was then sectioned at a location 40° into the bend and inspected visually and by dial gauge thickness techniques. The surface finish of the bore appeared to have been affected primarily on the outer half of its circumference, and a pattern of very shallow erosion undulations was noted, especially toward the lower (upstream) bend angles when viewed from the sectioned opening. The extrados of the elbow was then examined ultrasonically with an Aerotech 1/4-in. diameter, 25-MHz alpha transducer fitted with a short lucite delay line. A Branson 303B pulser-receiver with time-analog gate accessory was used, with the transducer assembly in direct contact with the elbow, to determine wall thickness as a function of bend angle. The agreement with dial-gauge results, where a comparison was feasible, was ± 0.0254 mm (1 mil). The 25-MHz results, combined with additional data from the integral extensions of the pipe beyond the bend, provided the basis for the wear profile shown in Fig. 3. The display of a peak at a location approximately one-quarter of the way through the bend was similar to the erosive profile of Elbow I,[4] but a second site of greater wear observed near 40° in Elbow I was not seen in Elbow II. If the erosion of Elbow II had con-

tinued, the relatively smooth curvature of the profile might have been obscured by surface undulations like those of Elbow I. The erosive exposure of Elbow II was reported by DOE personnel[5] at the Synthane plant. Coal throughput was 153700 kg (169 tons) (380 g/s max), and conveying gas was CO_2 plus steam at 3-15 m/s and 120-260°C mixed coal-plus-gas temperature.

Erosive wear of the stellite liner in the inlet zone of the HYGAS high-pressure cyclone separator after more than 3000 operating hours was described in the preceding quarterly report.[2] The results have been used (Fig. 4) to update the previously reported plot[3] of wear versus operating time of the cyclone. The wear data before the first inspection at 300 h had been obtained by linear extrapolation after the second survey at 518 h, and the estimate was improved (Fig. 4) in the light of the post-518-hour behavior. The 2304-h and 3396-h operating-time values are corrected[6] and supersede those of Refs. (2) and (3). The linear least-squares wear rate of the stellite liner was 0.012 mm/day (0.020 in./1000 h).

Repairs to connecting cables of the ANL erosive-wear detection system[2] at the Bi-Gas Pilot Plant have been made with the cooperation of plant personnel. The cables had been damaged after a burner rupture in February. The automatic scanning mode of the monitoring system will be tested during the next period of plant operation. The anticipated effect of pipe temperature on the indicated thickness will be verified, and the effects of any physical or electrical interference from the plant will be observed.

Efforts to improve the method of field attachment of ultrasonic waveguides to metallic transfer lines and fittings have continued. Site-to-site differences within the existing field installations in the amount of acoustic scattering from attachment welds have interfered with automatic scanning of the waveguide groups. The advice of ANL staff welding consultants[7] has been obtained, preliminary tests of attachment by percussion welding have been made, and a set of test samples prepared and electric-arc stud-welded by a commercial welding firm has been evaluated.

(Note: the electric-arc stud-welding method[8,9] was used to install waveguides at 31 sites at the Bi-Gas Pilot Plant and at all test points on the Synthane Mark II instrumented elbow. A stored-arc technique that had previously been favored[10] after laboratory tests of waveguide attachment to flat specimens was rejected when difficulties in attachment to piping were encountered in the field.)

A set of 16 waveguides was manufactured by Nelson Stud Welding Service (a division of TRW) in Lorain, Ohio, and electric-arc stud-welded there to test blocks that represented specimen materials. Well-characterized materials and best-effort procedures were used to determine whether the method or the field implementation needs improvement for this application. Nelson personnel emphasized that the inadvertent use of, e.g., Type 1113 rather than 1020 carbon steel or Type 303 rather than 304 stainless steel

might produce porous and unsuitable welds and that the most careful control of welding parameters is required to obtain welds of good acoustic transparency. The 16 test samples, shown in Fig. 5, consisted of six carbon steel waveguides of 9.5-cm (3/8-in.) diameter welded to carbon steel blocks; six stainless steel waveguides of 9.5-cm (3/8-in.) diameter welded to stainless steel blocks; and four carbon steel waveguides of 16-mm (5/8-in.) diameter welded to carbon steel blocks. A machined reference shoulder was provided on each waveguide a short distance ($\sim$ 6 mm) above the point of attachment to the block, and each waveguide was knurled above the shoulder to suppress acoustic reflections from the cylindrical surface.

The weld samples were evaluated for suitability as waveguide-attachment welds for an automatically scanned erosive-wear detection system. A satisfactory weld was defined as one from which the maximum pressure (oscilloscope pulse height) of the acoustic reflection was less than 20% of that from the normal, uneroded, short-specimen backwall. A 7.5-MHz, 3/8-in.-diameter transducer was used with a Branson 303B pulser-receiver for these tests. All twelve of the 9.5-mm (3/8-in.)-diameter samples were satisfactory, and none of the 16-mm (5/8-in.) diameter specimens were passable by the above definition. After consultation with the welding firm, it was decided to examine the larger-diameter specimens metallographically, and this work is in progress.

A review of the stainless steel welds in the field installations showed that about 60% were satisfactory, 20% were marginal because of multiple peaks from the weld, and 20% were not passable by the given definition. The carbon steel field welds will be evaluated during the next quarter.

It is concluded that several aspects of the welding method and the field implementation require further attention. Alternative methods that minimize the effect of attachment on the specimen material, including percussion welding, brazing, and mechanical techniques, will also be investigated.

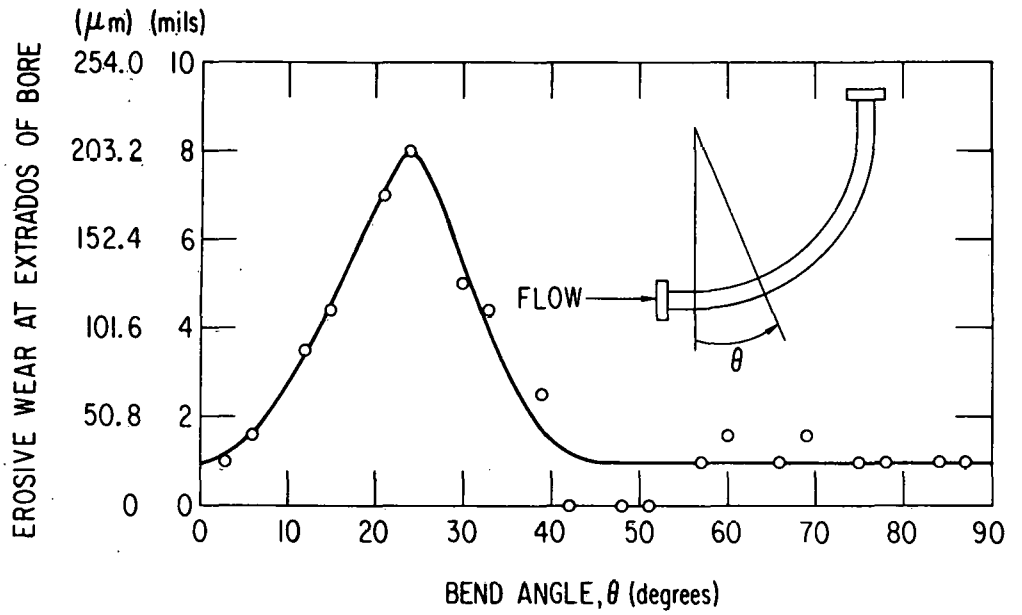

Fig. 3. Ultrasonically Determined Erosive Wear vs Bend Angle of Mark II Instrumented Elbow in Main Coal-feed Line of Synthane Pilot Plant. Estimated error band ± 25 μm (± 1 mil). Elbow: 90° bend of 0.3-m radius formed from 1-in. Schedule 80 Type 304 SS pipe. Coal throughput: 153700 kg (169 tons) (380 g/s max) of Illinois #6. Conveying gas: CO_2 plus steam at 3-15 m/s and 120-260°C mixed coal-plus-gas temperature. Neg. No. MSD 65528

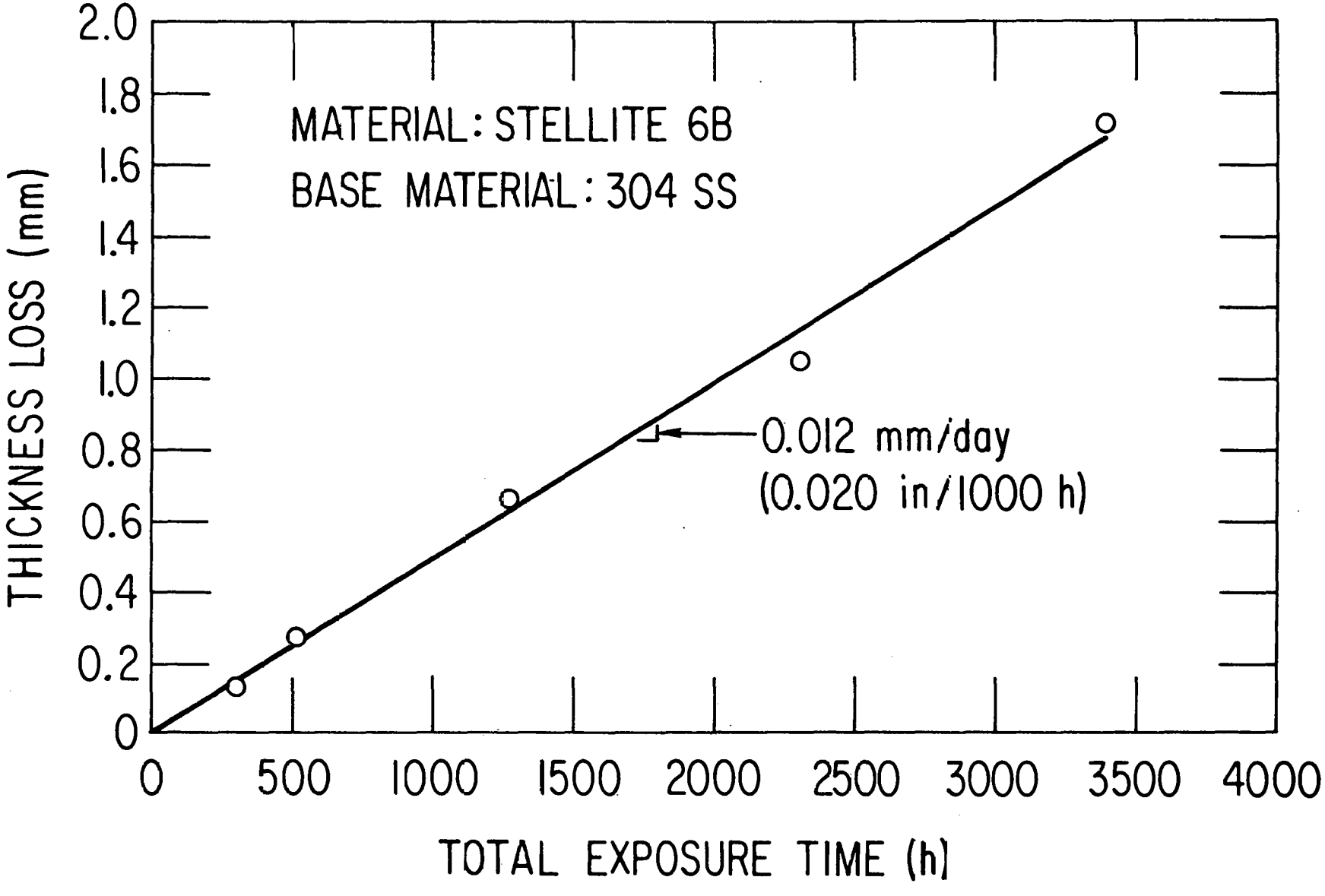

Fig. 4. Erosive Wear of HYGAS External Cyclone Determined by Ultrasonic Measurement. ANL Neg. No. 306-78-712

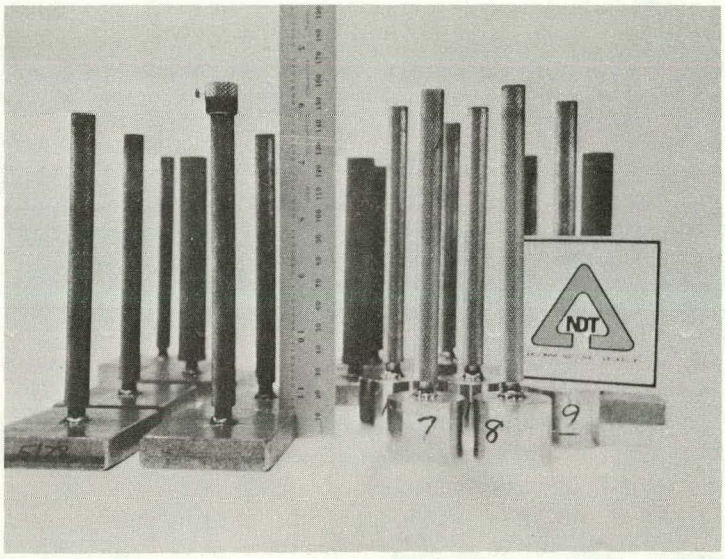

Fig. 5. Waveguides Electric-arc Stud-welded to Carbon Steel and Stainless Steel Blocks, Supplied as Attachment Weld Specimens by Nelson Stud Welding Service. ANL Neg. No. 306-78-713

(2) *Ultrasonic Studies - Scattering of Acoustic Waves from Rough Surfaces.* Initial studies on the effect of roughened surfaces on ultrasonic wall-thickness measurements were described last quarter.[2] During the present quarter, a major goal has been to improve the data acquisition and processing system. Figure 6 shows a schematic diagram and photographs of the system developed this quarter. The transducer is now controlled by a lathe bed which allows various scan rates across a surface with a positioning accuracy of about 30 μm. The transducer is mounted on a goniometer to allow accurate positioning.

The immersion transducer is operated in a pulse-echo mode with a gate used to select only the reflected echo. This is fed into a transient waveform recorder, the output of which is monitored on an oscilloscope to compare sampled output with analog input waveform. The transient recorder output is fed to a minicomputer for analysis.

The present program emphasizes scattering off the back surface, in contrast to previous studies[11,12] which focused attention on the front surface. Figure 7 shows the attenuation difference between the echos off the front and back surfaces. Figure 7a is the reflected echo off the front surface; Fig. 7b is the reflected echo off the back surface, which shows the ≈ 20-db attenuation caused by passage of the signal through the wall thickness. Figure 7c shows the echo reflected off the back surface, but with a gain adjustment to equalize the signal strengths between the two surfaces. Note the expected 180° phase reversal between the front and back surfaces.

Figures 8 through 10 show the effect of a roughened surface on the RF ultrasonic signal as well as the spectral content of the RF signal. Figure 8a (lower trace) shows the RF signal of the reflection off the front face. Figure 8b is the resultant frequency spectrum. Figure 9a (lower trace) is the RF of the reflected pulse off the front face of a periodically roughened surface with a 1/16" pitch, 60° cut and rounded peaks.[2] Figure 9b is the resultant frequency spectrum. Figure 10a (lower trace) is the RF signal obtained when the periodically roughened surface is turned over so that the signal of interest is on the back side. Figure 10b is the resultant frequency spectrum of 10a. The initial data suggest a significant difference in the frequency spectrum for the signal scattered from the back as opposed to the front surface.

During the next quarter, a more complete analysis of these results, as well as a comparison with several other periodically roughened surfaces, will be performed.

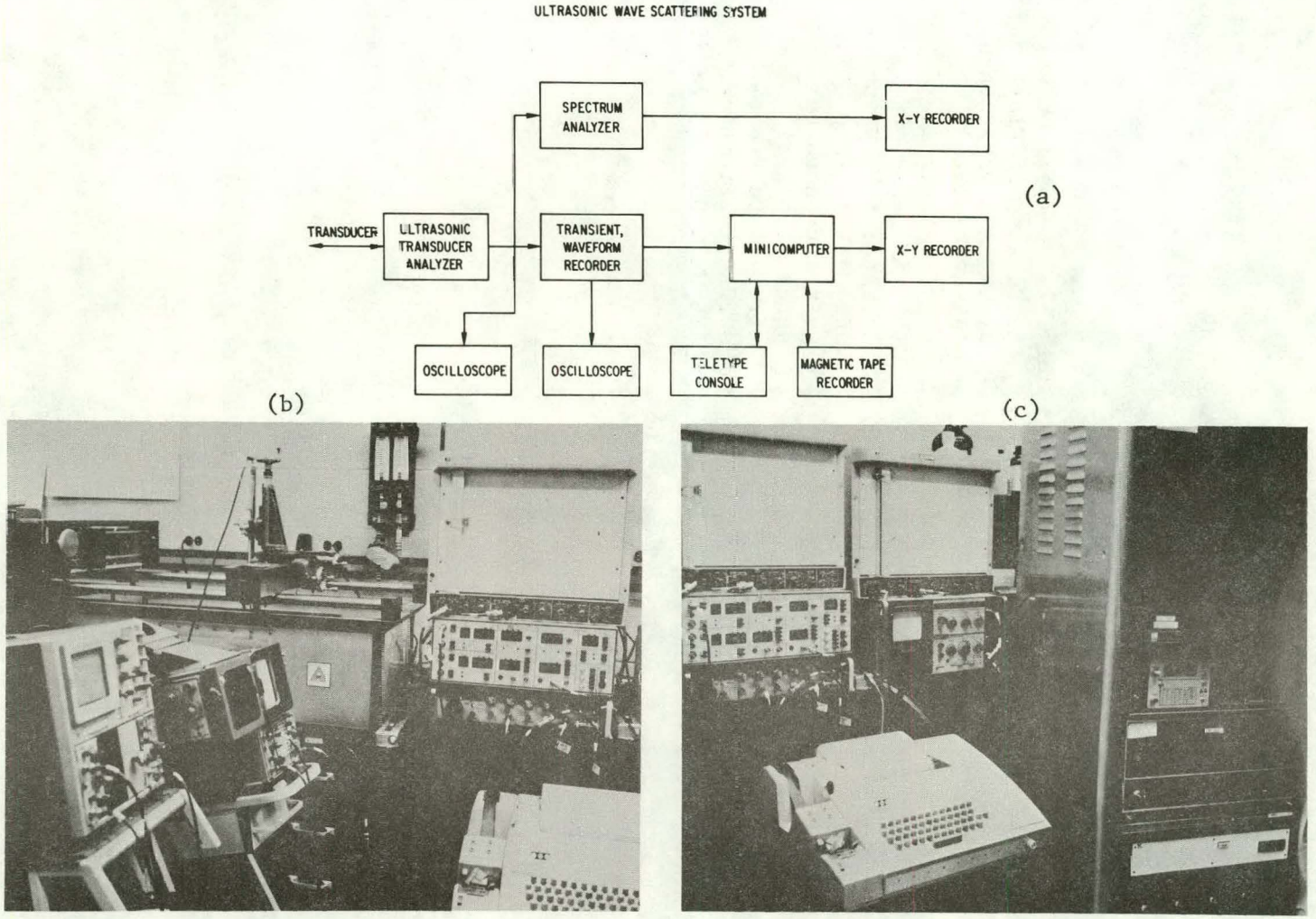

Fig. 6. Ultrasonic Wave-scattering Data Acquisition and Processing System. (a) Schematic of the system; (b) photograph of the water tank and lathe bed; (c) photograph of the minicomputer, transient recorder and spectrum analyzer. ANL Neg. No. 306-78-799

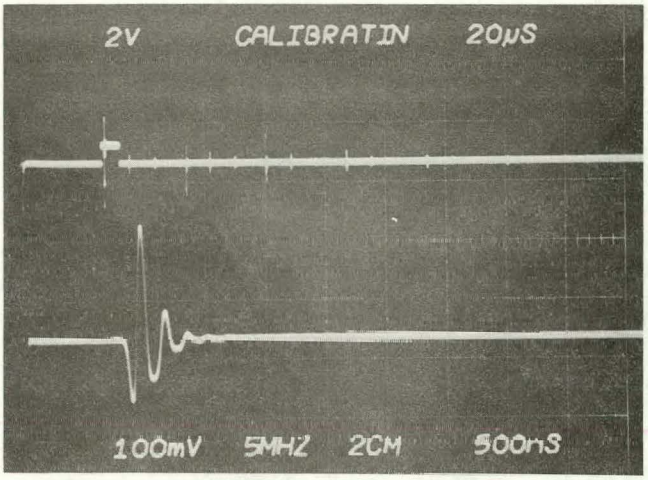

(a)

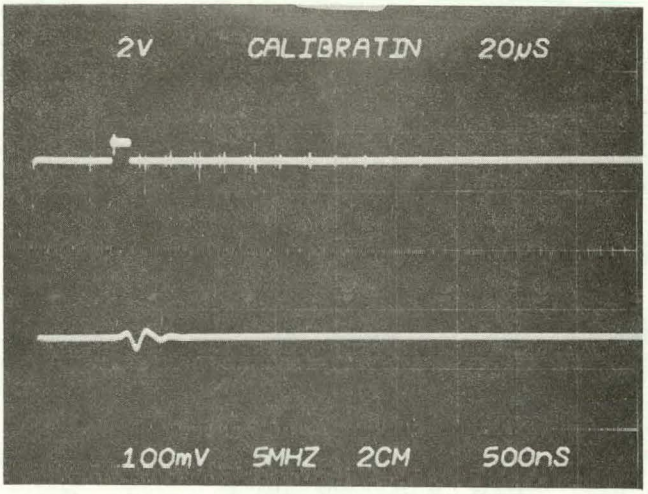

(b)

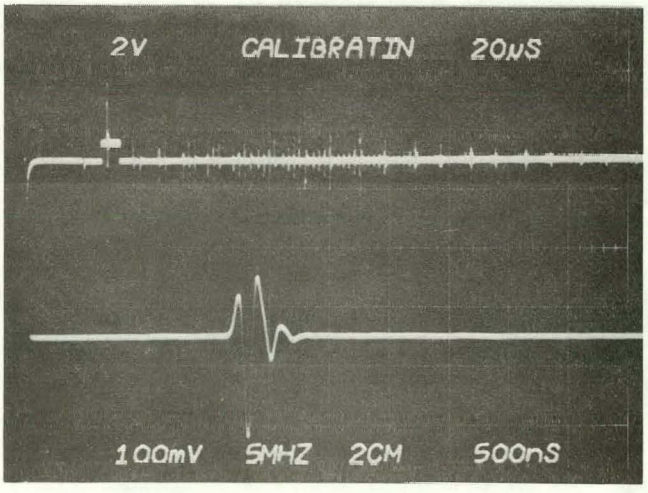

(c)

Fig. 7. Comparison of RF Pulses Off Flat Block in a Water Bath. (a) RF pulse off front surface; (b) RF pulse off back surface; (c) RF pulse off back surface, with gain increased to equalize signal strength to front-surface reflection. ANL Neg. No. 306-78-751

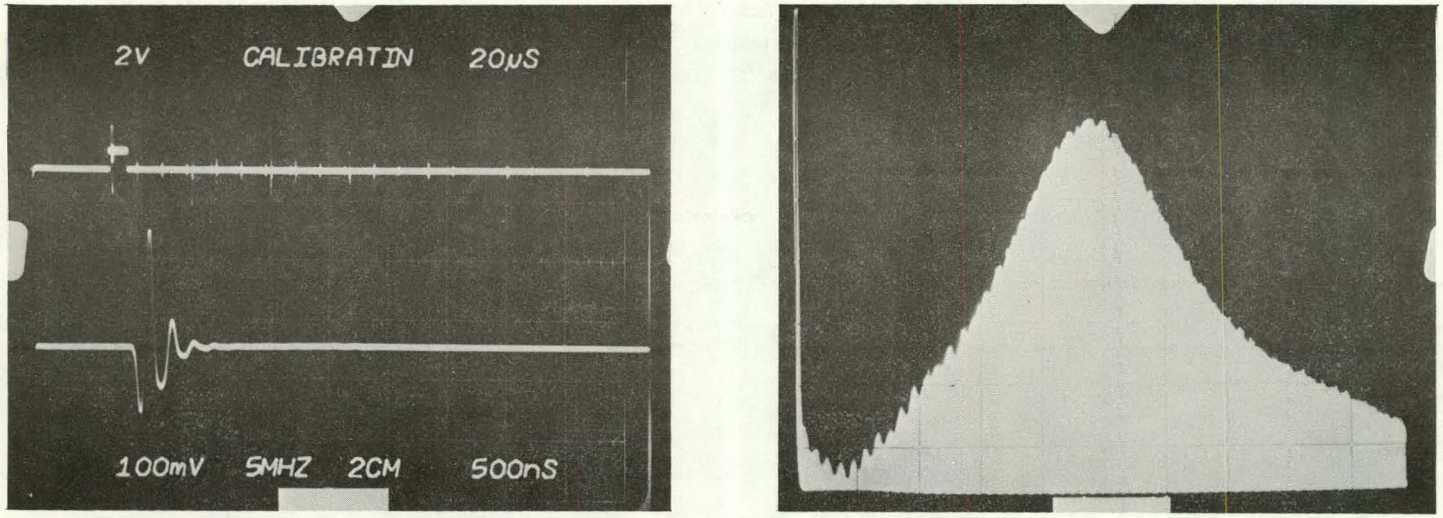

Fig. 8. RF and Resultant Frequency Spectrum of Reflected Pulse from Front Flat Surface using 1/2", 5-MHz Immersion Transducer. (a) RF pulse; (b) resultant frequency spectrum: Horizontal sweep 1 MHz/div, center frequency 5 MHz. ANL Neg. No. 306-78-754

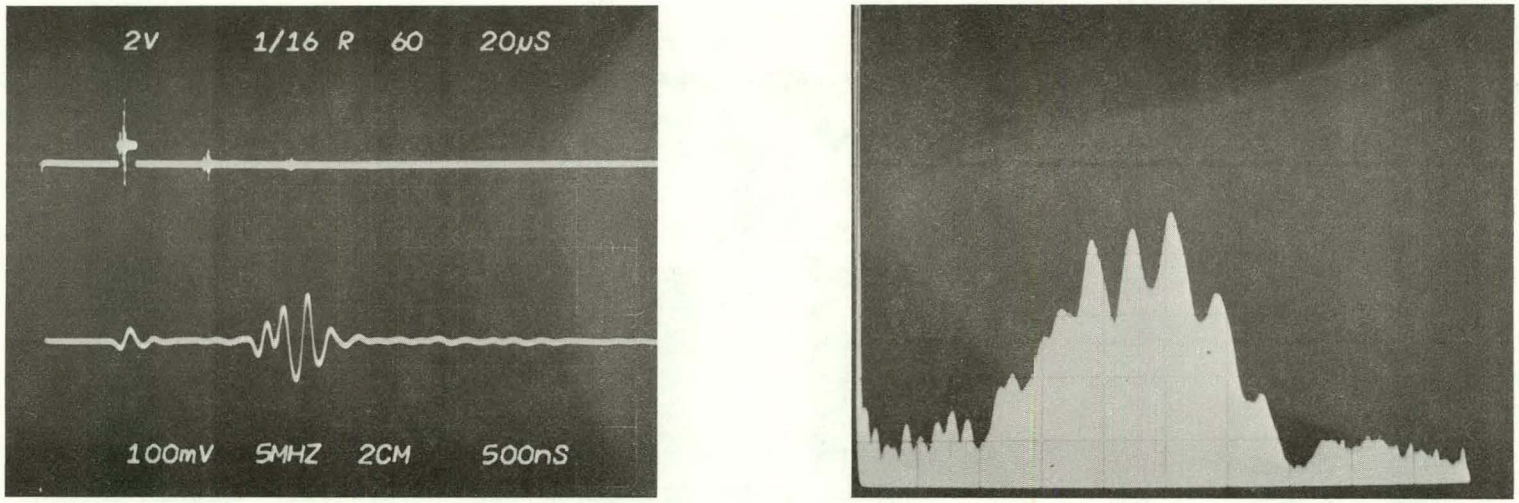

(a) (b)

Fig. 9. RF and Resultant Frequency Spectrum of Front-reflected Echo Off Periodically Roughened Surface Using 1/2", 5-MHz Immersion Transducer. (a) RF pulse; (b) resultant frequency spectrum 1 MHz/div, 5 MHz center frequency. ANL Neg. No. 306-78-753

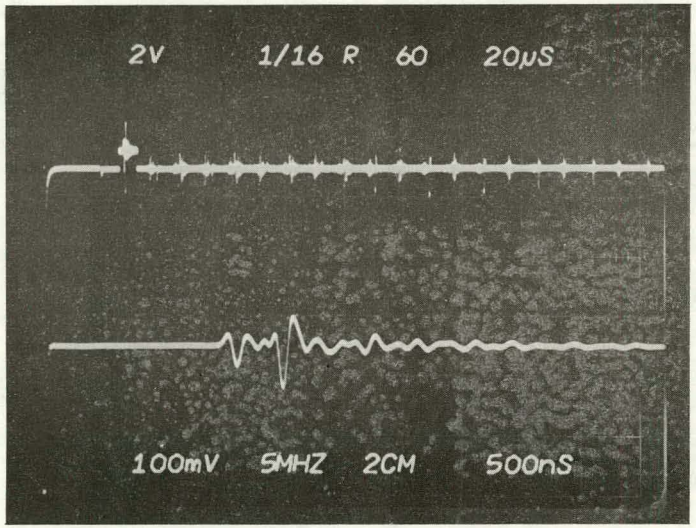

(a)

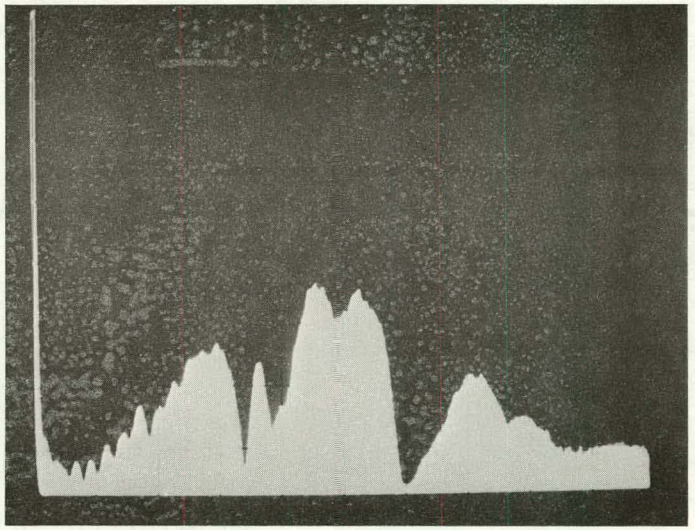

(b)

Fig. 10. RF and Resultant Frequency Spectrum of Back-reflected Echo Off Periodically Roughened Surface Using 1/2", 5-MHz Immersion Transducer. (a) RF pulse; (b) resultant frequency spectrum 1 MHz/div, 5 MHz center frequency. ANL Neg. No. 306-78-752

2. Refractory Installation Practices

a. Detection of Thermally Induced Acoustics from Refractory Materials

During the current quarter, analysis has continued on the acoustic emission obtained from the two high-alumina panels fired last quarter at two different heating rates. During the last quarter, ringdown counts, count rate and characteristic slope were initially evaluated as parameters to discriminate between the two panel tests.[2] To date, acoustic-emission data suggest that no frequency window is present in any phase of the thermomechanical degradation which takes place during initial heating and cooling. Figure 11 shows the total ringdown count for each panel for both the broadband and resonant (175-KHz) transducers. To be noted from this figure is the essentially identical tracking of acoustic emissions by both transducers during both tests. The resonant transducer yields higher actual total counts, but this transducer is also ∿ 30 db more sensitive than the broadband transducer. Figure 11 also compares individual event counts with ringdown counts for both transducers and both panels. Again, the event counts track the ringdown counts very closely. This suggests little difference between the events which occurred during these two firings. This is supported by visual inspection of the surfaces. Figures 12 and 13 show mappings of the crack patterns observed on each panel. No large cracks are observed on either panel and the crack widths are essentially the same on each panel. The difference between the panels seems to be related to the timing of the events as opposed to the kinds of events which occurred. This is easily seen in Figures 14 and 15 which show total ringdown counts as a function of hot-face temperature for the resonant and broadband transducers, respectively.

Further, the thermal "kaiser"-type effect previously observed on uniformly heated small laboratory samples is observed in these large-panel tests. Figures 14 and 15 show that increases in counts do not occur until the previous maximum temperature has been surpassed. Panel II shows this more markedly because two temperature drops occurred during the heating schedule.

Figures 16 and 17 are plots of the characteristic slope value as a function of temperature for panels I and II, respectively; data for both resonant and broadband transducers are shown. These results support previous findings by others, which indicated that a uniform shift in amplitude distribution should not affect the slope. A strong correlation is evident between the resonant and broadband transducer data at various temperatures, even though the broadband transducer has less sensitivity and hence a different amplitude distribution. Additionally, the characteristic slope values for the two panels are qualitatively similar, except that lower values were observed for panel II during heating and for panel I at maximum temperature and when cooling began.

During the next quarter, a panel will be thermally shocked to generate large faults for characterization by acoustic-emissions techniques.

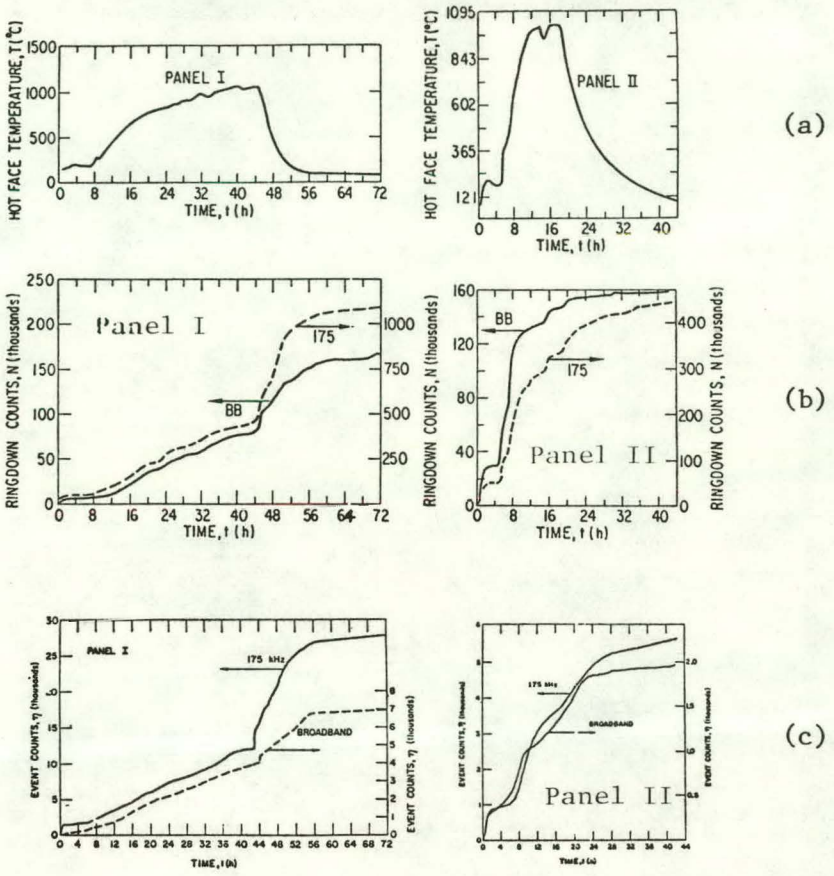

Fig. 11. Comparison of Ringdown Counts and Individual Event Counts as a Function of Time during the Firing Schedule for Two High-alumina (95% Al_2O_3) Panels Heated at Different Heating Rates. (a) Hot-face temperature profile for panels I and II; (b) ringdown counts for 175-KHz and broadband transducers for panels I and II; (c) event counts for 175-KHz and broadband transducers for panels I and II. Neg. No. MSD 65495

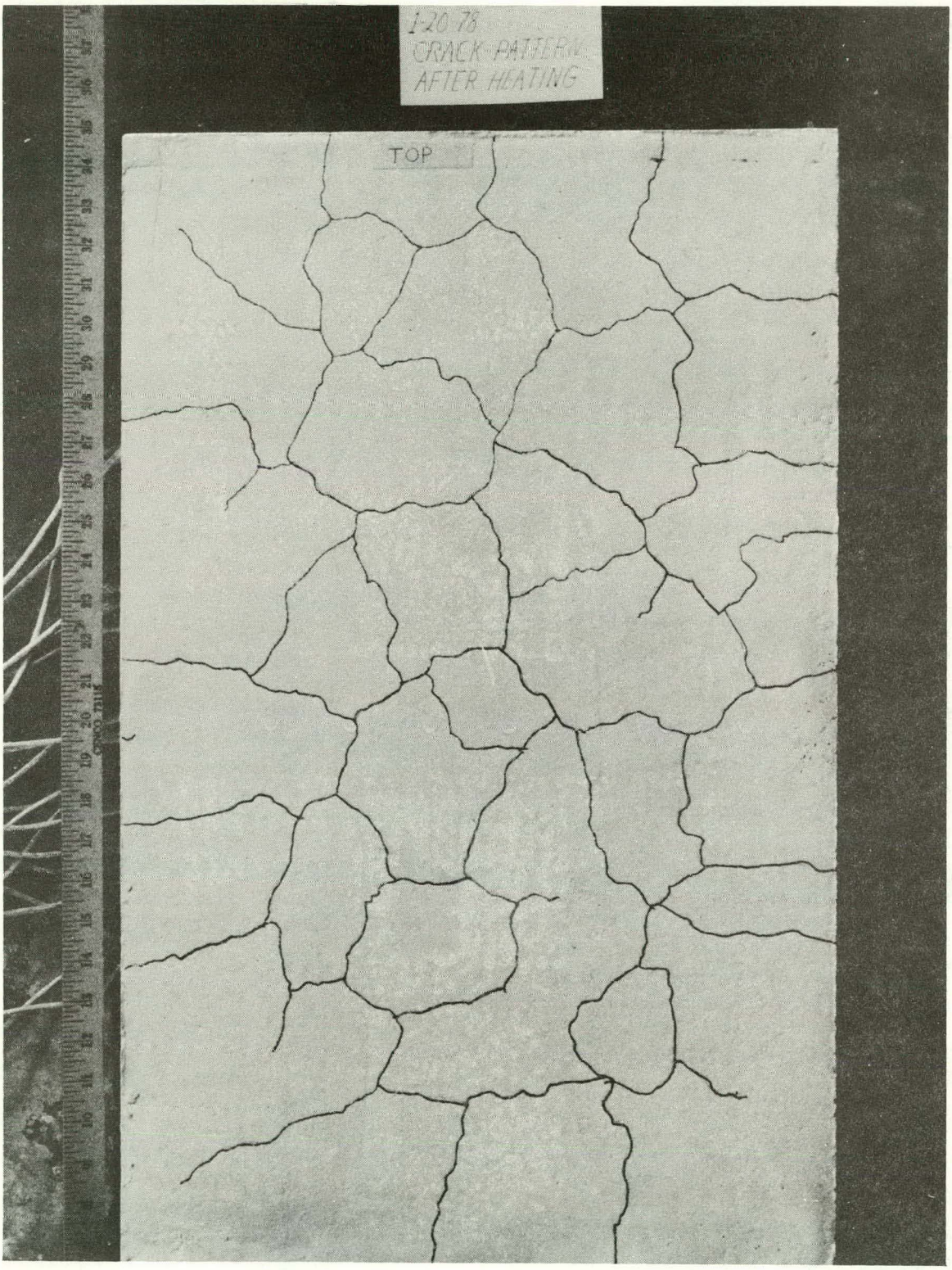

Fig. 12. Crack Pattern Observed on Face of Panel I after Heating and Cooling. Neg. No. MSD65478

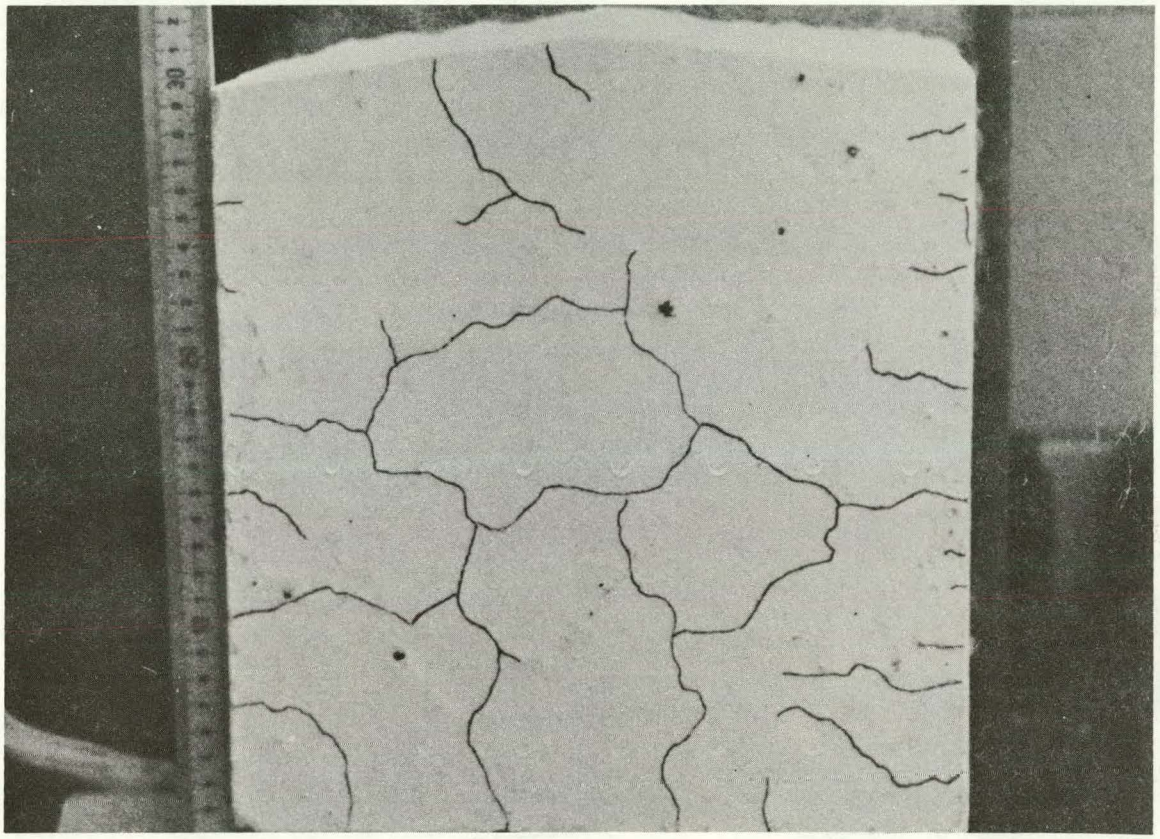

Fig. 13. Crack Pattern Observed on Panel II after Heating and Cooling. Neg. No. MSD 65477

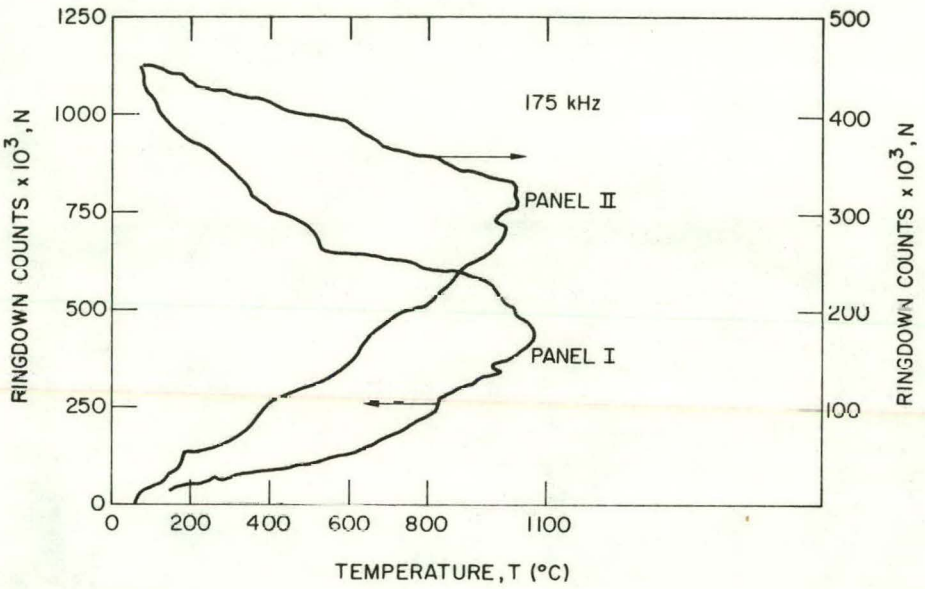

Fig. 14. Comparison of Ringdown Counts for Panel I and Panel II as a Function of Hot-face Temperature (175-KHz Transducer). ANL Neg. No. 306-78-718

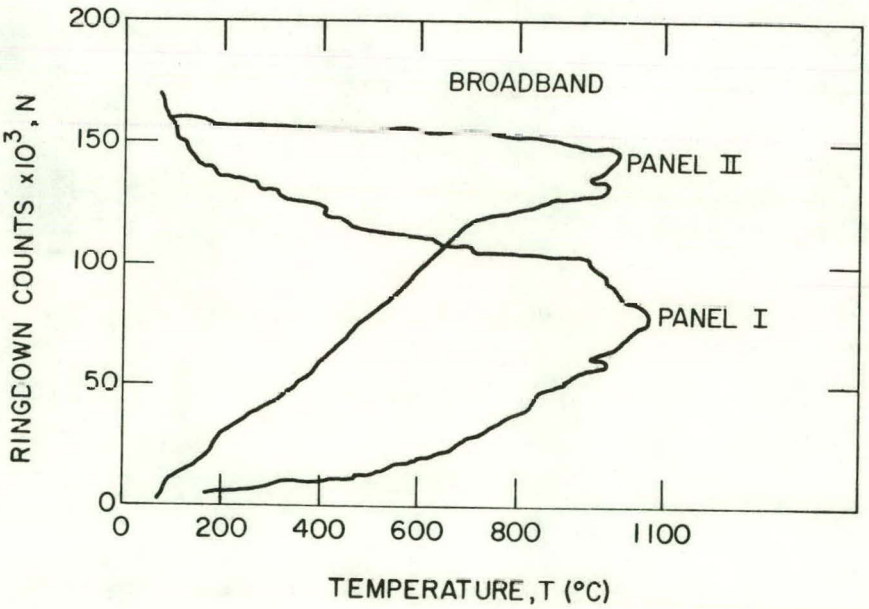

Fig. 15. Comparison of Ringdown Counts for Panel I and Panel II as a Function of Hot-face Temperature (Broadband Transducer). ANL Neg. No. 306-78-717

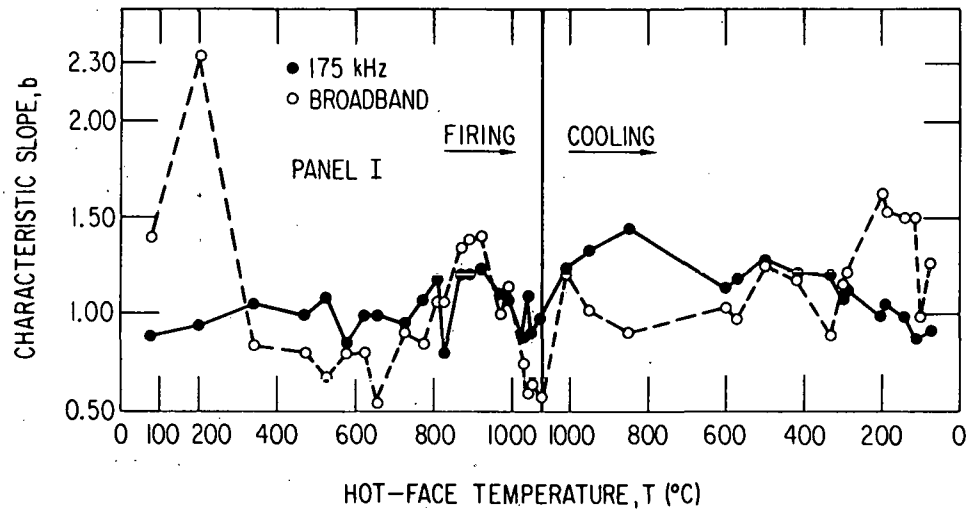

Fig. 16. Comparison of Characteristic Slope Values for 175-KHz and Broadband Transducers as a Function of the Hot-face Temperature (Panel I). ANL Neg. No. 306-78-716

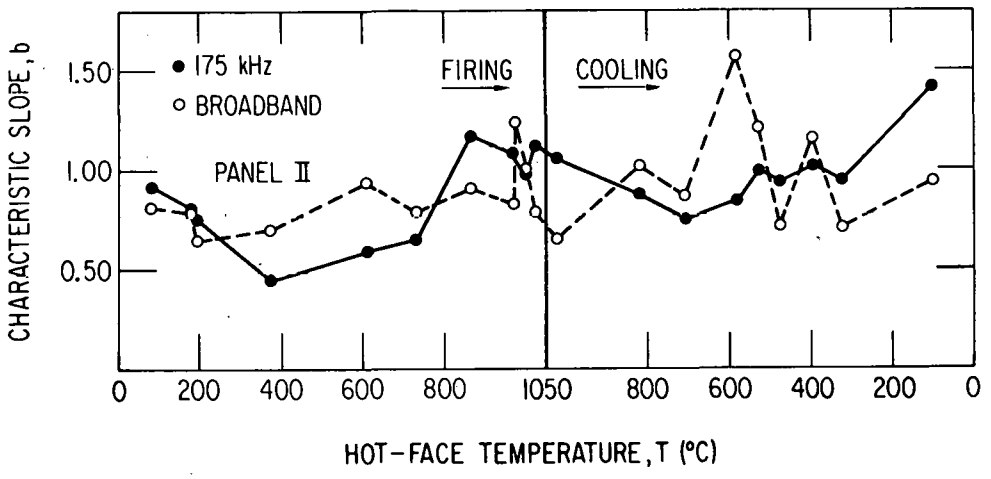

Fig. 17. Comparison of Characteristic Slope Values for 175-KHz and Broadband Transducers as a Function of the Hot-face Temperature (Panel II). ANL Neg. No. 306-78-715

3. Component Inspection

a. Acoustic Monitoring of Valves

During this quarter a visit was made to the Naval Ship Research and Development Center at Annapolis, Maryland to discuss the status and scope of the Navy Acoustic Valve Leak Detection Program and possible areas of cooperation between our programs.

The Navy program has explored three areas of application: (1) low-ΔP water valves, (2) high-ΔP steam and air valves, and (3) high-ΔP hydraulic fluid valves (ΔP is the pressure drop across the valve). The water-valve program has been underway for approximately five years. The Navy currently utilizes commercially available transducers (Endevco 2213 low-g-level accelerometers) and an electronics package of its own design. The electronics unit permits either a spectral scan within the range 10-100 KHz or a simple RMS readout of the acoustic output. Virtually all in-field inspections by the Navy have been carried out using RMS measurements. The package also includes a band-pass filter ($\sim$ 5 KHz) with a selectable center frequency which can vary between 10 and 100 KHz. Water-valve inspections are usually carried out at fairly low frequencies ($\sim$ 25 KHz). For high-pressure air valves, somewhat higher frequencies ($\sim$ 50 KHz) have been used.

The Navy has agreed to supply one of their devices for testing at the Morgantown Energy Research Center Valve Test Facility. Acoustic Emission Technology Corp. will supply a prototype version of its AET 204B, which was developed to meet ANL specifications for a leak-detection system. The AET 204B is a wide-bandwidth system (1 KHz-2MHz) with a selectable narrow-bandwidth filter. Center frequencies of 175, 375, and 750 KHz are available in the prototype unit.

The two units cover a wide frequency range. The relatively low-frequency unit developed by the Navy should offer greater sensitivity at low leakage levels than the higher-frequency ANL system, but it will also be susceptible to structure-borne background noise. More extensive field testing will be required to evaluate the relative merits of the two approaches.

Field testing of the two devices at the MERC valve-test facility will be conducted during the next quarter with the cooperation of Mr. John Gardner, Project Engineer at MERC. The initial installation will occur in late July. Preliminary testing will be carried out for approximately one month to establish test procedures and ensure compatibility with other MERC test objectives. Longer-term tests will then be undertaken to establish threshold values of acoustic output for unacceptable leakage levels and to investigate the possibility of quantitative correlations between acoustic output and leakage levels.

Task D -- Corrosion Behavior of Materials in Coal-conversion Processes
(K. Natesan)

The objectives of this program are to (1) develop uniaxial tensile data on four commercial alloys exposed to multicompnent gas environments, (2) experimentally evaluate the high-temperature corrosion behavior of iron- and nickel-base alloys in gas environments with a wide range of oxygen, sulfur and carbon potentials, and (3) develop a systems approach based upon available thermodynamic and kinetic information so that possible corrosion problems in different coal-conversion processes can be evaluated.

The experimental program used to generate uniaxial tensile data on four iron- and nickel-base alloys exposed to multicomponent gas environments was discussed in detail in an earlier report.[14] A description of the experimental system and the chemical composition of the alloys and gas mixtures used in the program were given in the last quarterly report.[2] The calculated values for the oxygen and sulfur partial pressures established by the gas mixtures in different runs are listed in Table III.

During the present quarter, 3.6-Ms (1000-h) exposures of corrosion and uniaxial tensile specimens to gas mixtures 2A at 871°C, 3A at 871 and 750°C, and 1B at 750°C were completed. Postexposure tensile tests of the specimens were conducted in vacuum at an initial strain rate of 4.1×10^{-4} s^{-1}. The load-elongation data from the tensile tests were converted to true stress-true strain curves for the alloys in the as-received condition and after exposure to the multicomponent gas environments. In general, the flow stress of the material decreases after exposure to complex gas mixtures when compared with that of the material in the as-received condition. The engineering tensile properties, such as 0.2% yield stress, ultimate tensile strength (UTS), uniform strain, and total elongation were also evaluated from the load-elongation data. Tables IV and V show listings of these properties for the alloys in the as-received condition and after 3.6-Ms (1000-h) exposures to complex gas mixtures at test temperatures of 750 and 871°C, respectively. The results show that preexposure of the materials to multicomponent gas mixtures results in a decrease in 0.2% yield stress and UTS with only minimal changes in the uniform strain over the range of $\sim$ 4 to 13%.

After the mechanical tests were completed, the cross sections and fracture surfaces of uniaxial tensile specimens were examined by SEM with an energy-dispersive x-ray analyzer. Figures 18-21 show SEM photographs of the cross sections of Incoloy 800, Type 310 stainless steel, Inconel 671, and U.S. Steel Alloy 18-18-2, respectively, after a 3.6-Ms exposure to a complex gas mixture (run B03A750). Also shown in these figures are the metallic-element (chromium, iron, nickel, and silicon) and sulfur distributions in the scale/alloy interface regions of the samples. The photographs show that the scales developed on Incoloy 800 and Type 310 stainless steel in run B03A750 are predominantly Cr-rich oxide; very little sulfur was detected. The thickness of the oxide scale in these specimens was $\sim$ 5 μm and the depth of internally affected zones was $\sim$ 25 μm. Inconel 671 also developed

an oxide scale ∿ 5 μm in thickness, as well as an ∿ 25-μm thick external sulfide scale. The U.S. Steel Alloy 18-18-2 developed only a sulfide scale in the environment of run BO3A750. The scale thickness and depth of the internally affected zone were ∿ 50 and 20 μm, respectively. Examination of the specimens from other experiments is in progress.

Additional experiments are under way to evaluate the effect of variations in the exposure environment on the uniaxial tensile behavior of the selected alloys.

TABLE I. Partial Pressures of Oxygen and Sulfur Used in Different Experimental Runs

Gas Mixture, vol. %						Run No.	Temperature, °C	P_{O_2}, atm[a]	P_{S_2}, atm
CO	CO_2	CH_4	H_2	H_2O	H_2S				
11.7	15.4	10.0	13.0	48.9	1.0	A01A750	750	1.7×10^{-20}	3.8×10^{-8}
						A01A871	871	1.1×10^{-17}	4.0×10^{-7}
						A01A982	982	1.3×10^{-15}	2.4×10^{-6}
17.3	11.5	10.0	23.0	37.2	1.0	E12A750	750	5.9×10^{-21}	2.7×10^{-8}
						E12A871	871	3.6×10^{-18}	2.7×10^{-7}
						E12A982	982	4.5×10^{-16}	1.5×10^{-6}
26.0	14.9	10.0	26.0	22.1	1.0	B03A750	750	2.2×10^{-21}	2.9×10^{-8}
						B03A871	871	1.4×10^{-18}	2.8×10^{-7}
						B03A982	982	1.8×10^{-16}	1.6×10^{-6}
9.1	12.0	30.0	10.0	37.9	1.0	C01B750	750	6.7×10^{-22}	9.9×10^{-9}
						C01B871	871	3.2×10^{-19}	8.7×10^{-8}
						C01B982	982	3.9×10^{-17}	4.8×10^{-7}
13.4	8.9	30.0	17.8	28.9	1.0	F02B750	750	1.9×10^{-22}	9.7×10^{-9}
						F02B871	871	5.0×10^{-20}	7.6×10^{-8}
						F02B982	982	5.4×10^{-18}	4.1×10^{-7}
20.1	11.5	30.0	20.1	17.3	1.0	D03B750	750	1.9×10^{-22}	1.1×10^{-8}
						D03B871	871	4.9×10^{-21}	8.6×10^{-8}
						D03B982	982	4.2×10^{-20}	4.4×10^{-7}

[a]Conversion factor: 1 atm = 0.101 MPa.

TABLE II. Uniaxial Tensile Properties of Four Alloys in the As-received Condition and After 3.6-Ms Exposures to Multicomponent Gas Environments at 750°C

Alloy	Treatment	0.2% Yield Stress, MPa	Ultimate Tensile Strength, MPa	Uniform Strain, %	Total Elongation, %
Incoloy 800	As-received	91.0	226.7	4	136
	A01A750	53.3	204.2	10.8	100.4
	E12A750	40.5	200.0	8.8	70.4
	B03A750	69.9	190.3	13.3	90.0
	C01B750	64.6	138.2	8.6	55.4
Type 310 Stainless Steel	As-received	49.2	257.9	4	38
	A01A750	43.2	219.4	8.1	36.4
	E12A750	36.1	222.9	9.4	27.5
	B03A750	-	216.0	7.4	38.9
	C01B750	-	188.9	7.9	29.0
U.S. Steel Alloy 18-18-2	As-received	63.5	191.2	8	70
	A01A750	57.6	181.9	12.3	64.5
	E12A750	43.7	182.5	9.8	62.5
	B03A750	-	163.9	6.9	43.8
	C01B750	-	171.5	8.4	58.1
Inconel 671	As-received	49.2	339.0	9	32
	A01A750	48.5	265.3	3.9	77
	E12A750	45.1	256.9	5.9	54.1
	B03A750	-	223.5	3.9	107.3
	C01B750	-	241.7	4.3	98.4

TABLE III. Uniaxial Tensile Properties of Four Alloys in the As-received Condition and After 3.6-Ms Exposures to Multicomponent Gas Environments at 871°C

Alloy	Treatment	0.2% Yield Stress, MPa	Ultimate Tensile Strength, MPa	Uniform Strain, %	Total Elongation, %
Incoloy 800	As-received	30.7	119.7	4	123
	A01A871		Sample Embrittled		
	E12A871	41.3	75.7	2.5	46.4
	B03A871	60.2	100.0	7.9	149.6
Type 310 Stainless Steel	As-received	43.0	138.5	3	48
	A01A871	20.0	106.5	8.9	76
	E12A871		Sample Embrittled		
	B03A871		Sample Embrittled		
U.S. Steel Alloy 18-18-2	As-received	36.8	94.5	3	71
	A01A871		Sample Corroded		
	E12A871		Sample Embrittled		
	B03A871		Sample Embrittled		
Inconel 671	As-received	42.0	141.1	5	87
	A01A871	27.3	105.9	4.9	172
	E12A871	43.1	88.9	3.5	74.3
	B03A871	62.2	118.0	3.0	163.0

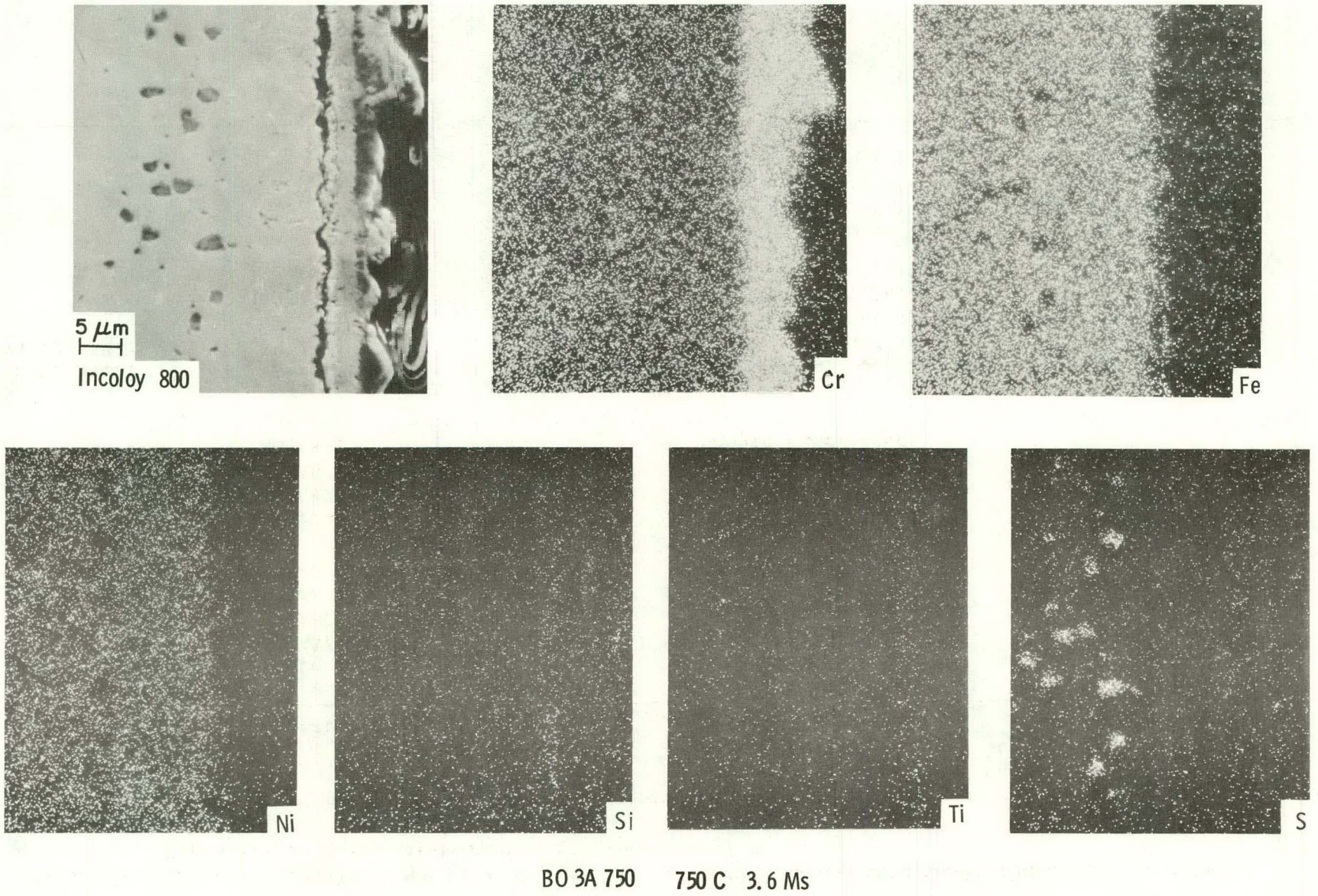

Fig. 18. X-ray Photograph and Cr, Fe, Ni, Si, Ti, and S Distribution in Incoloy 800 Specimen After a 3.6-Ms Exposure to a Complex Gas Mixture at 750°C (Run BO3A750). In the distribution pictures, light regions indicate high concentrations of the respective elements. ANL Neg. No. 306-78-704

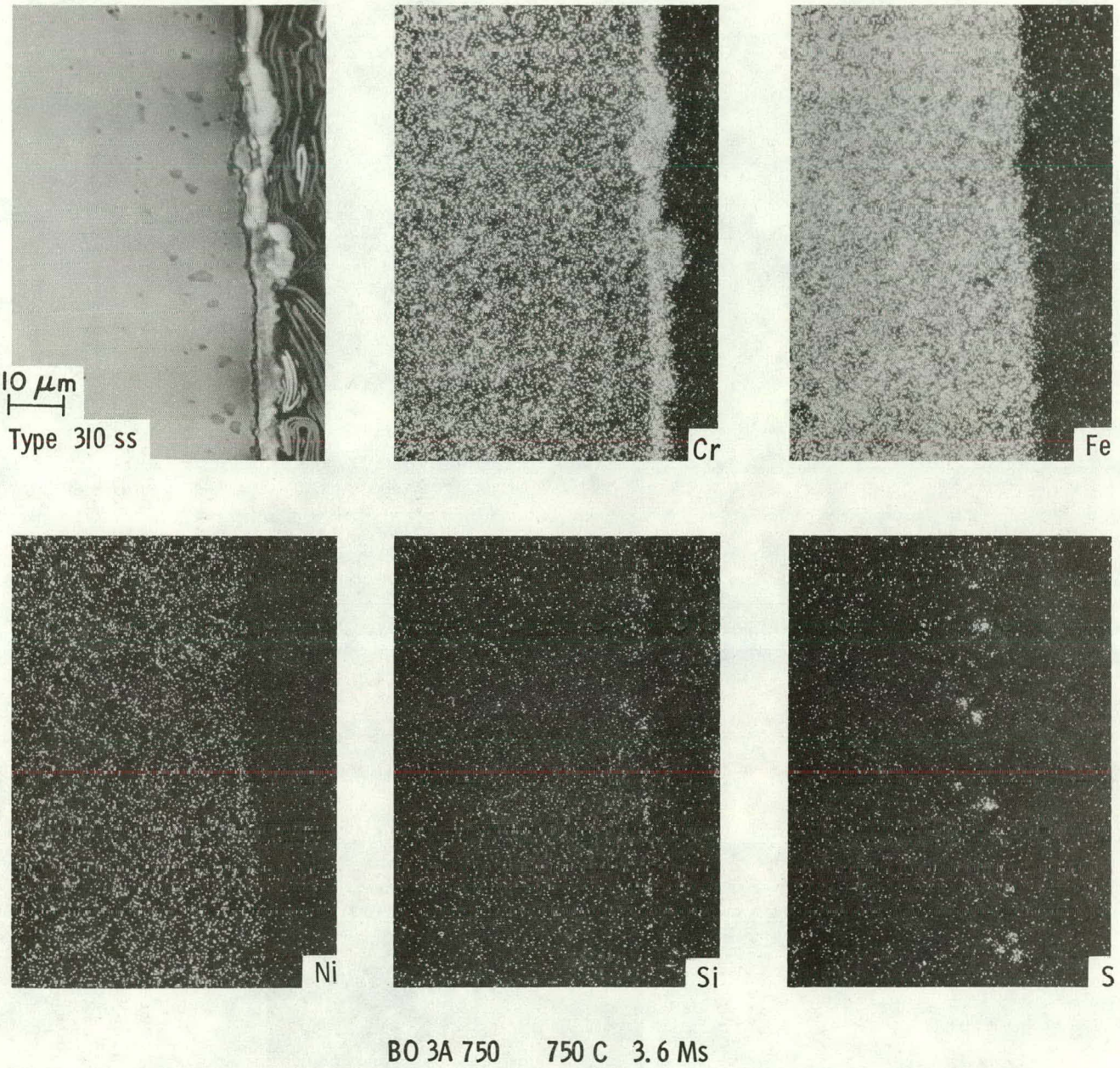

Fig. 19. X-ray Photograph and Cr, Fe, Ni, Si, and S Distribution in Type 310 Stainless Steel Specimen After a 3.6-Ms Exposure to a Complex Gas Mixture at 750°C (Run BO3A750). In the distribution pictures, light regions indicate high concentrations of the respective elements. ANL Neg. No. 306-78-703

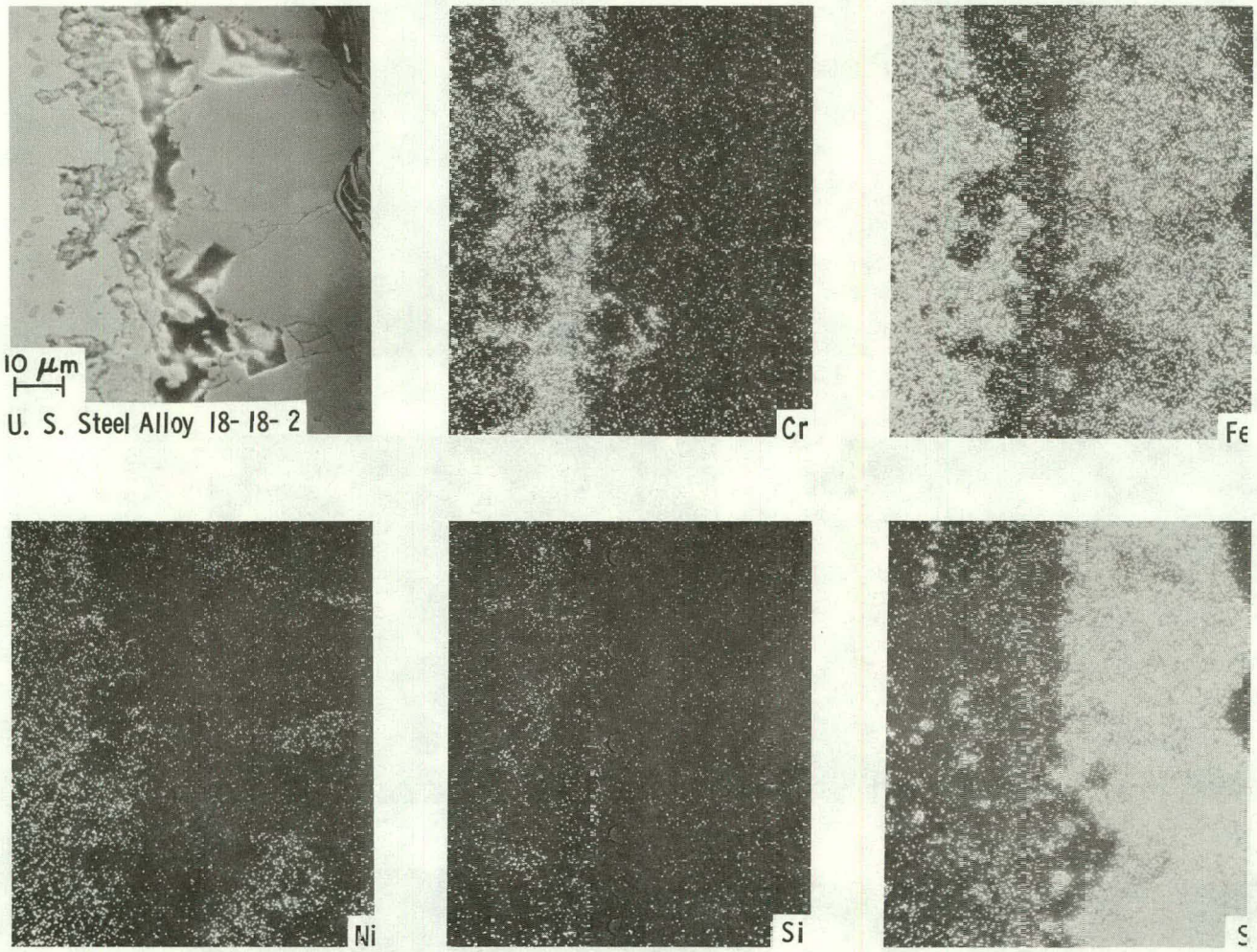

Fig. 20. X-ray Photograph and Cr, Fe, Ni, Si, and S Distribution in U.S. Steel Alloy 18-18-2 Specimen After a 3.6-Ms Exposure to a Complex Gas Mixture at 750°C (Run BO3A750). In the distribution pictures, light regions indicate high concentrations of the respective elements.
ANL Neg. No. 306-78-699

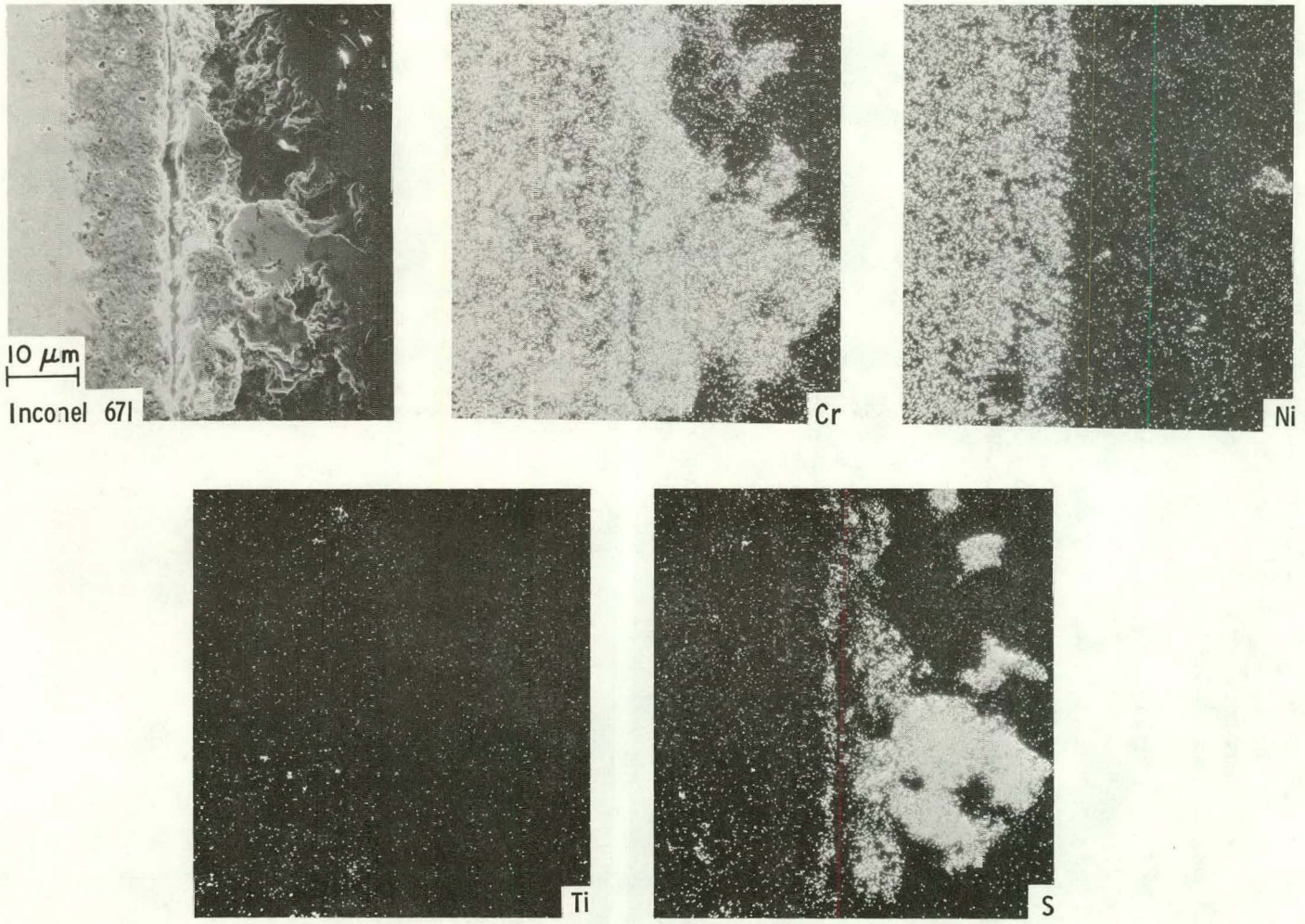

Fig. 21. X-ray Photograph and Cr, Ni, Ti, and S Distribution in Inconel 671 Specimen After a 3.6-Ms Exposure to a Complex Gas Mixture at 750°C (Run BO3A750). In the distribution pictures, light regions indicate high concentrations of the respective elements.
ANL Neg. No. 306-78-697

Task E -- Erosion Behavior of Materials in Coal-conversion Processes
(J.Y. Park and W.J. Shack)

During this quarter, work has continued on the installation and refurbishing of the high-temperature erosion-test apparatus. The particle-feeding, environmental control, and heating systems have been installed, and preliminary room-temperature erosion tests and high-temperature corrosion tests will begin next quarter.

High-speed motion pictures of the moving particles have been made using the Redlake Hi-cam camera. Frame-by-frame analysis of the film was carried out to obtain particle velocities and trajectories. The distribution of velocities for a group of fifteen particles is shown in Fig. 22. The particle trajectories can be described in terms of the relative angle ϕ between the particle path and the rotor arm. The distribution of the angle ϕ for the particles analyzed is shown in Fig. 23. The average velocity and angle ϕ are

$$V = 24.2 \pm 1.4 \text{ m/s}$$

$$\phi = 36° \pm 5° \qquad (1)$$

for a rotor speed f = 1000 rpm. The ϕ component of the velocity of the particle is simply $V_\phi = \omega r$ where ω is the angular velocity of the rotor and r is the distance along the rotor. The equation of motion for the particle is then

$$\frac{d^2r}{dt^2} + 2\mu\omega \frac{dr}{dt} + \omega^2 r = 0 \qquad (2)$$

where μ is the coefficient of friction between the particle and the rotor and t is time. Rewriting this equation in terms of the velocity $V_r = dr/dt$ and changing independent variables from t to r yields

$$V_r \frac{dV_r}{dr} + 2\mu\omega V_r = \omega^2 r \qquad (3)$$

Solving this differential equation for V_r and evaluating the results for r = R, the point at which the particle leaves the rotor, gives

$$V_r = \omega[(1+\mu^2)^{1/2} - \mu] \qquad (4)$$

The particle velocity and path angle ϕ are then

$$V = (V_r^2 + V_\phi^2)^{1/2} = \sqrt{2}\,\omega R[1 + \mu^2 - \mu(1 + \mu)^{1/2}]^{1/2} \qquad (5)$$

$$\phi = \tan^{-1}(V_r/V\phi) = (1 + \mu^2)^{1/2} - \mu \qquad (6)$$

Substituting the experimentally measured value of ϕ into (5), the effective coefficient of friction μ is found to be

$$\mu \simeq 0.32 \qquad (7)$$

This value is in good agreement with the usual value obtained for sliding friction between steel and lead. The theoretical results [Eqs. (5) and (6)] indicate that the velocity V is proportional to the rotor frequency and the angle ϕ is independent of frequency. Using the experimental results [Eq. (1)] to evaluate the constant of proportionality gives

$$V = 0.0242f \pm 0.0014f \text{ m/s} \qquad (8)$$

$$\phi = 36° \pm 5°$$

where $f = \omega/2\pi$ is the rotational frequency in revolutions per minute (r/min).

Room-temperature erosion tests were performed in the ANL low-temperature apparatus in an air environment on Type 304 stainless steel, 1015 carbon steel, Incoloy 800, Type 310 stainless steel, Alloy 671, and Stellite 6B using 60 μm Al_2O_3 particles with an impact velocity of 70 m/s and impingement angles of 15°, 20°, 25°, 45°, and 90°. The mass loss vs mass impacted curves for each of these materials are shown in Figs. 24-29. It is clear from these figures that a steady-state erosion rate (mass loss/mass impacted) has been reached, and that the mass loss is proportional to the mass impacted. Figure 30 shows the erosion rate as a function of the angle of impact for the different materials. One somewhat surprising result is that under these conditions, Stellite 6B, a standard erosion-resistant hard-facing material, outperforms ordinary 1015 carbon steel only at low angles of impact. Table VI shows the rank ordering of materials at low and high angles of impact in terms of their erosion resistance. It should be emphasized that this ordering may be valid only for the specific set of environmental conditions chosen for this test. These tests will be used as benchmarks for the high-temperature erosion apparatus during room-temperature test runs.

TABLE IV. Relative Erosion Resistance of Structural Materials

	Low Angle of Impact (15°)	High Angle of Impact (90°)
Most Resistant	Stellite 6B	1015 Carbon Steel
	1015 Carbon Steel	Incoloy 800
	Inconel 671	Inconel 671
	Type 304 SS	Type 304 SS
	Incoloy 800	Stellite 6B
Least Resistant	Type 310 SS	Type 310 SS

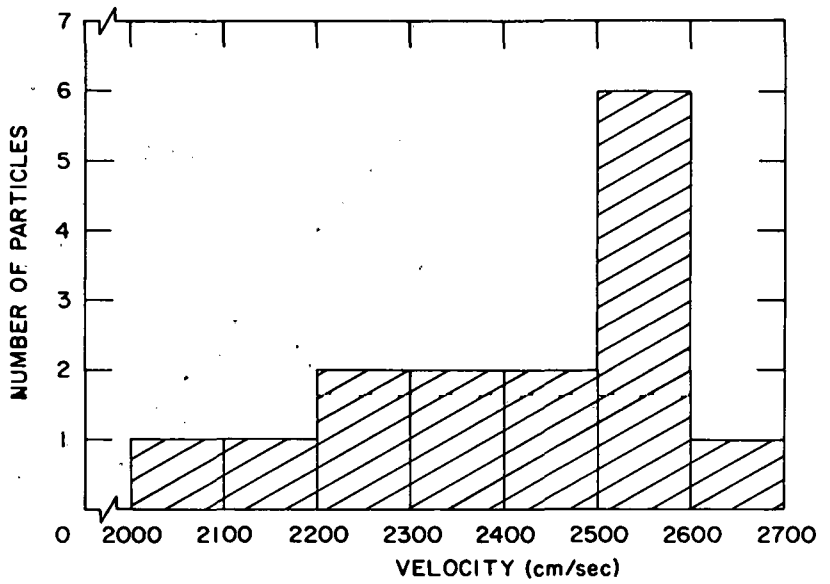

Fig. 22. Distribution of Particle Velocites in Erosion Apparatus. ANL Neg. No. 306-78-760

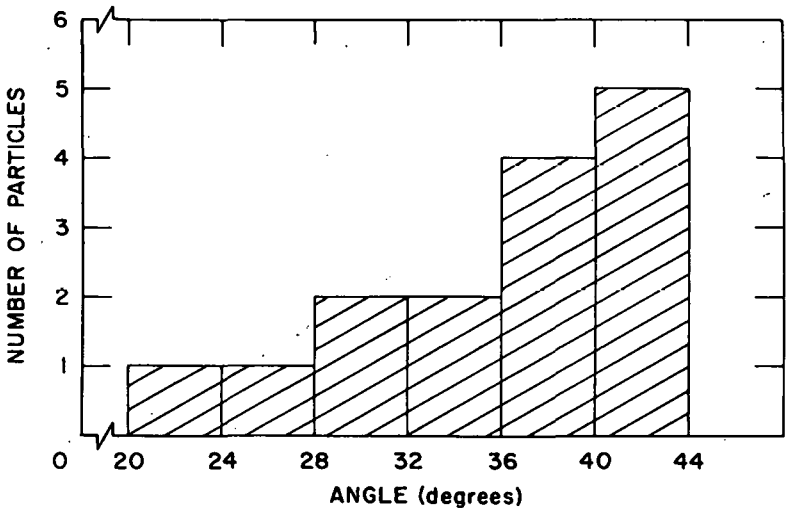

Fig. 23. Distribution of the Angle ϕ between the Particle Path and Rotor Arm. ANL Neg. No. 306-78-761

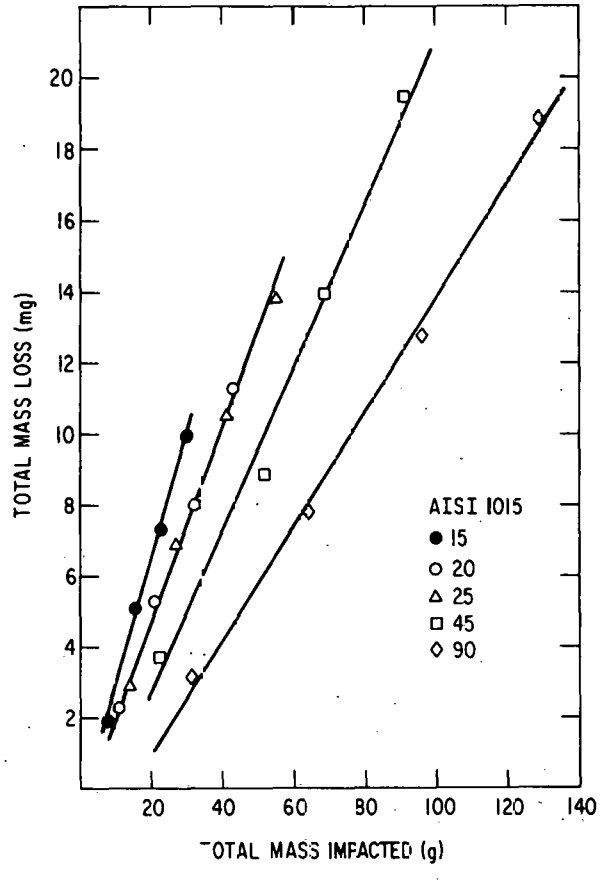

Fig. 24. Mass Loss of 1015 Carbon Steel as a Function of the Total Mass of Erodant Impacted. ANL Neg. No. 306-78-762

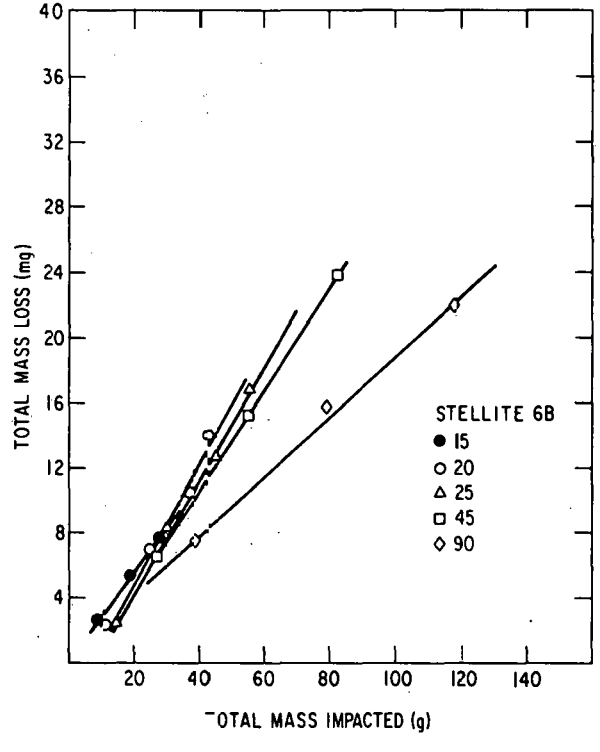

Fig. 25. Mass Loss of Stellite 6B as a Function of the Total Mass of Erodant Impacted. ANL Neg. No. 306-78-759

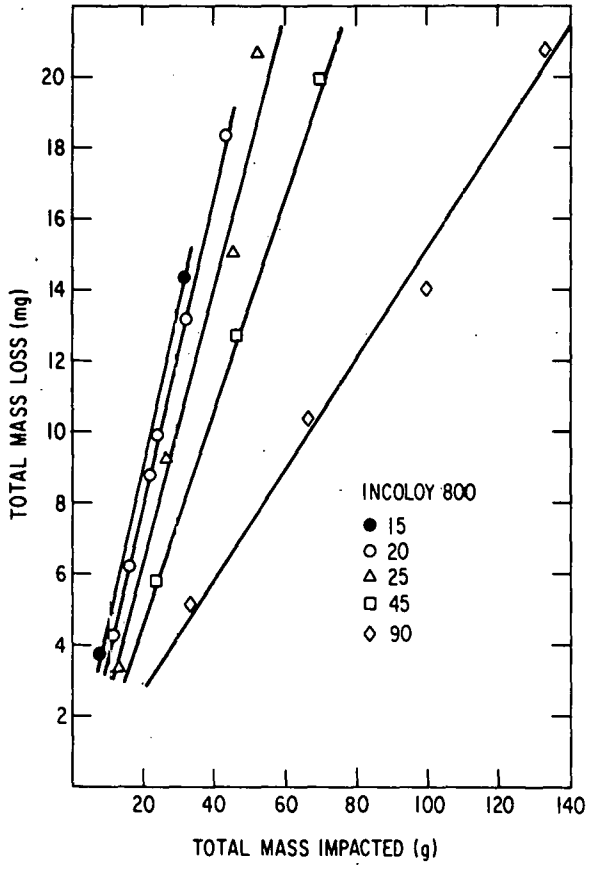

Fig. 26. Mass Loss of Incoloy 800 as a Function of the Total Mass of Erodant Impacted. ANL Neg. No. 306-78-763

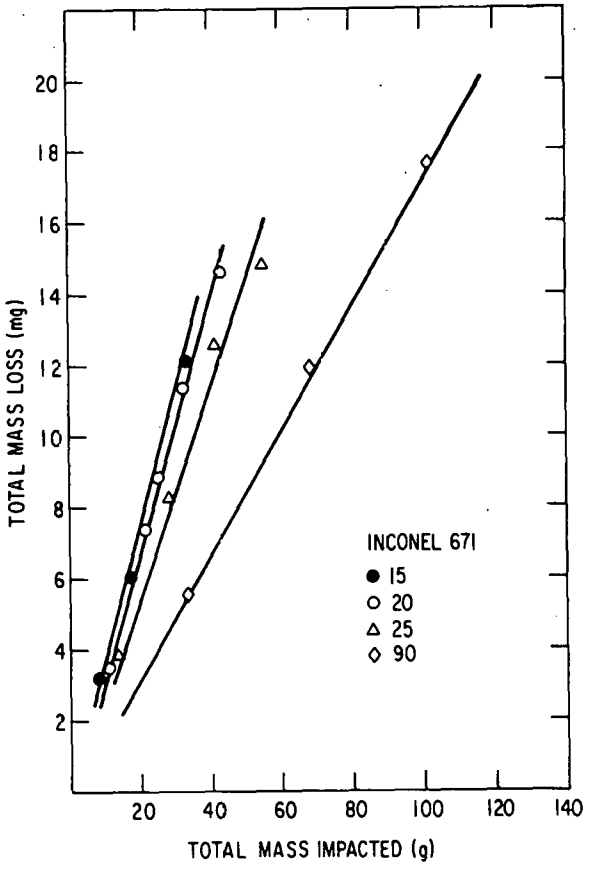

Fig. 27. Mass Loss of Inconel 671 as a Function of the Total Mass of Erodant Impacted. ANL Neg. No. 306-78-764

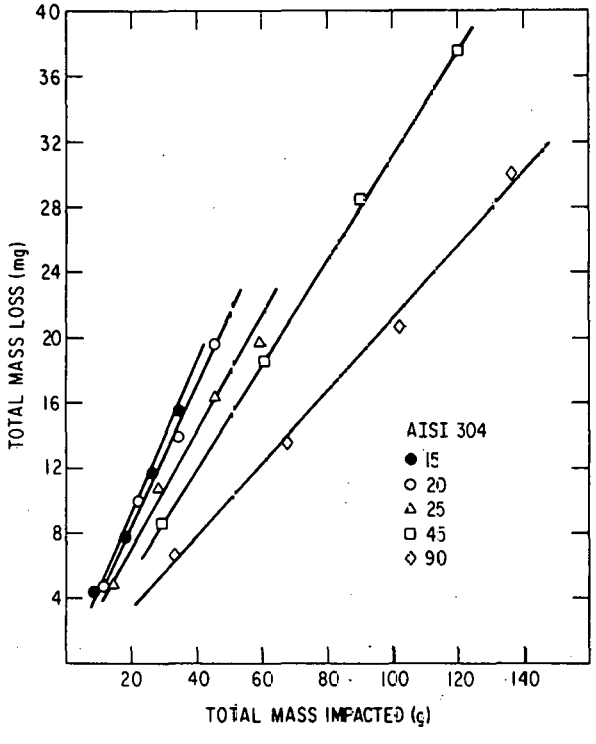

Fig. 28. Mass Loss of Type 304 Stainless Steel as a Function of the Total Mass of Erodant Impacted. ANL Neg. No. 306-78-758

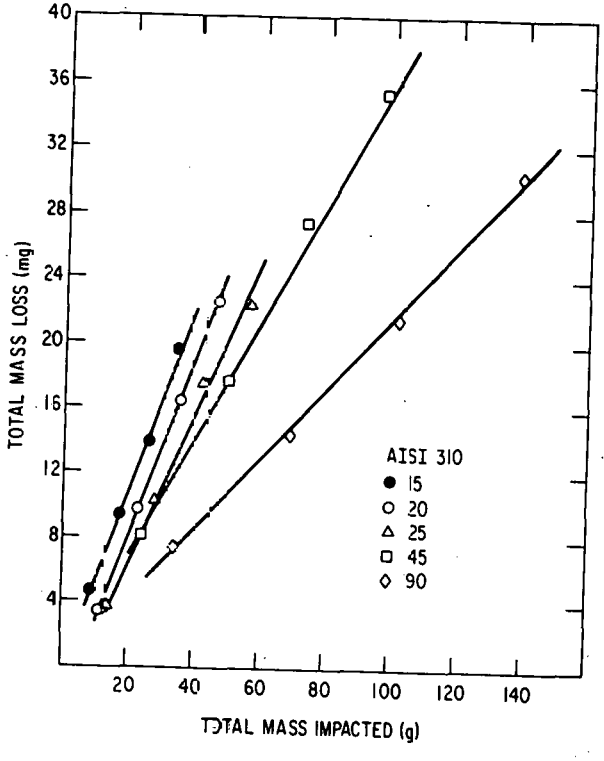

Fig. 29. Mass Loss of Type 310 Stainless Steel as a Function of the Total Mass of Erodant Impacted. ANL Neg. No. 306-78-765

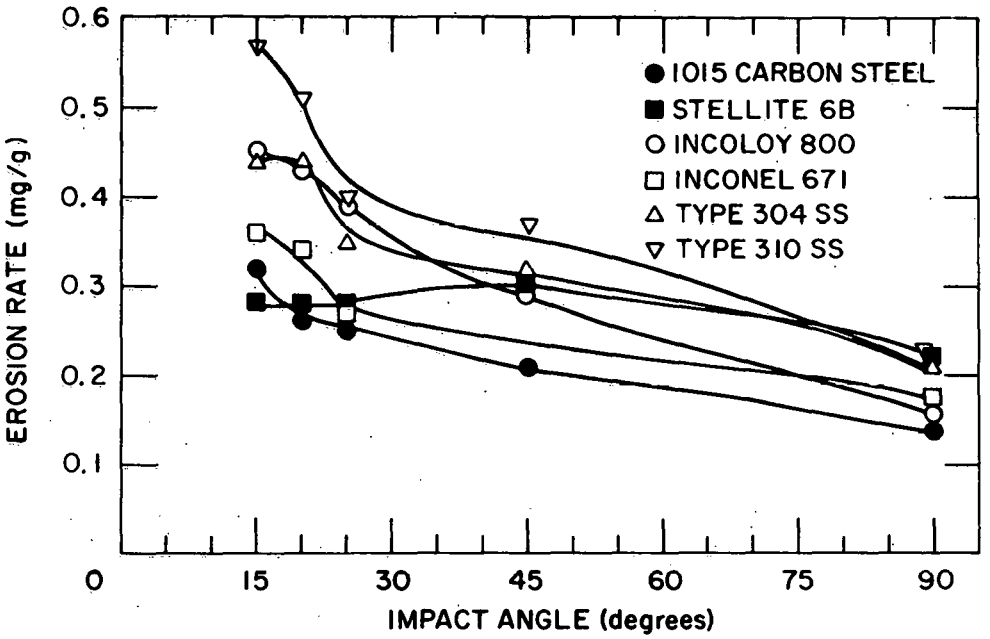

Fig. 30. Erosive Wear Rate as a Function of Particle Impact Angle. ANL Neg. No. 306-78-766

Task F -- Component Performance and Failure Analysis *(S. Danyluk, G.M. Dragel, L. Pahis, J.Y. Park, M. Nimalendran, S. Greenberg, J.C. Florek, J. Wang, S. Mihailovich, R.H. Lee)*

The activity during this quarter involved examination of components from the Synthane pilot plant and the HYGAS Ash Agglomerating Gasifier. The results of these analyses are presented in Tables VII and VIII.

TABLE V. Failed Components from the Synthane Coal Gasification Pilot Plant

Component	Material	Failure Cause	Recommendation
CO_2-compressor unloading fingers	Unknown	Erosion	
Eighth-floor oxygen line	316 stainless steel	Chloride-assisted stress-cracking; material not within manufacturer's specification	Replace line with material within specification; eliminate chlorides
Steam heat-up line	304 stainless steel	Intergranular chloride-assisted stress-corrosion cracking	Eliminate chlorides
Raw-gas scrubber	Carbon steel	Erosion-corrosion combination	Correct eccentricity of the flange. Replace the elbow in the upper stream with Ni-hardened iron casting pipe; monitor pipe-wall thinning with NDT techniques
Char-transfer line	Carbon steel	Erosion-corrosion combination	Replace section at the reducer end with Ni-hardened iron casting pipe
Oxygen line (#1203)	304L stainless steel	Pitting corrosion due to crud deposition	Use Type 316 stainless steel; use weld-neck reducer
Oxygen line (#1381)	304 stainless	Pitting; probably chlorides	Eliminate chlorides; use Type 316 stainless steel

TABLE VI. Failed Components from the HYGAS Ash Agglomerating Gasifier Coal-Gasification Pilot Plant

Component	Material	Failure Cause	Recommendation
Dipleg	310 stainless steel	Corrosion; erosion; operation above design operating temperature range	Operate within specified temperature range; restrain the dipleg from vibrating
Thermowell	310 stainless steel	Corrosion; operation above design operating temperature range	Coat OD with alumina; operate within specified temperature range
Pressure Tap	310 stainless steel	Corrosion; erosion; operation above design operating temperature range	Coat OD with stellite 6B: operate within specified temperature range

REFERENCES

1. T.F. Berry, W.C. Allen, and R.B. Snov, "Chemical Changes in Basic Brick During Service," J. Amer. Ceram. Soc. 33(4), 121-132 (1950).

2. Materials Technology for Coal-conversion Processes, Thirteenth Quarterly Report, January-March 1978, Argonne National Laboratory, ANL-78-54.

3. Materials Technology for Coal-conversion Processes, Eleventh Quarterly Report, April-June 1977, Argonne National Laboratory, ANL-77-62, p. 30.

4. Materials Technology for Coal-conversion Processes, Twelfth Report, July-December 1977, Argonne National Laboratory, ANL-78-6, pp. 19-20.

5. D. Dubis, Synthane Pilot Plant, personal communication (March 24, 1978).

6. J. Jones, HYGAS Pilot Plant, personal communication (July 6, 1978).

7. D.E. Walker and M.A. Pugatz, Argonne National Laboratory, personal communications (1978).

8. Metals Handbook, Vol. 6, 8th Ed., p. 167, American Society for Metals (1971).

9. Welding Handbook, Vol. 2, 7th Ed., Chapter 8, "Stud Welding", American Welding Society (1978).

10. Materials Science Division Coal Technology Fifth Quarterly Report, October-December 1975, Argonne National Laboratory, ANL-76-22, p. 26.

11. deBilly, M., Doucet, J., and Quentin, G.J., "Angular Dependence of the Backscattered Intensity of Acoustic Waves from Rough Surfaces", Ultrasonics International 1975, Vol. 11-2.

12. Quentin, G., deBilly, M., Cohen-Tenoudju, F., Doucet, J., and Jungman, A., "Experimental Results on the Scattering of Ultrasound by Randomly or Periodically Rough Surfaces in the Frequency Range 2 to 25 MHz", 1975 Ultrasonics Symposium Proceedings, IEEE Cat. No. 75 CHO 994-4SU, pp. 102-106.

13. D.E.W. Stone and P.F. Dingwall, "Acoustic Emission Parameters and Their Interpretation", NDT International, April 1977, pp. 51-59.

14. Materials Science Division Coal Technology Ninth Quarterly Report, October-December, 1976, Argonne National Laboratory, ANL-77-5.

Distribution of ANL-78-79

Internal:

E. G. Pewitt
R. G. Matlock
B. R. T. Frost
R. W. Weeks (6)
M. F. Adams
O. K. Chopra
S. Danyluk
D. R. Diercks
W. A. Ellingson (6)
J. Fischer
K. J. Reimann
C. A. Youngdahl
A. A. Jonke
T. F. Kassner
C. R. Kennedy
K. Natesan
E. L. Hartig
J. Y. Park
R. B. Poeppel
W. J. Shack
A. B. Krisciunas
ANL Contract Copy
ANL Libraries (5)
TIS Files (6)

External:

DOE-TIC, for distribution per UC-90c (276)
Manager, Chicago Operations Office
Chief, Office of Patent Counsel, CH
President, Argonne Universities Association
Materials Science Division Review Committee:
- E. A. Aitken, General Electric Co., Sunnyvale
- G. S. Ansell, Rensselaer Polytechnic Inst.
- R. W. Balluffi, Massachusetts Inst. Technology
- R. J. Birgeneau, Massachusetts Inst. Technology
- S. L. Cooper, Univ. Wisconsin
- C. Laird, Univ. Pennsylvania
- M. T. Simnad, General Atomic
- C. T. Tomizuka, U. Arizona
- A. R. C. Westwood, Martin Marietta Laboratories

R. R. Adams, Battelle Columbus Laboratories
E. M. Anderson, The Babcock & Wilcox Company
W. G. Bair, Inst. of Gas Technology
W. Bakker, USDOE/FE
J. A. Brooks, Amoco Oil Co., Naperville, Ill.
S. Carson, CE Lummus Co., Bruceton, Pa.
W. C. Corder, Battelle Columbus Laboratories
M. Crowley, Standard Oil of Indiana, Naperville, Ill.
J. Flagg, Universal Oil Products Co., Des Plaines, Ill.
E. Fox, Stearns-Roger Corp., Homer City, Pa.
H. E. Frankel, USDOE/FE
S. M. Gaitonde, Commonwealth Edison Co., Maywood, Ill.
D. Glaser, Stearns-Roger Corp. Denver
H. Heysteck, Tuscallosa Metallurgy Research Center, University, Ala.
V. Hill, IIT Research Inst.
D. Hull, Phillips Petroleum Co., Homer City, Pa.
R. I. Jaffeee, Electric Power Research Institute
D. L. Keairns, Westinghouse Research Labs.
H. Leavenworth, Albany Metallurgy Research Center
A. V. Levey, Lawrence Berkeley Laboratory
R. Lewis Synthane Pilot Plant, USDOE/FE, Pittsburgh
G. Long, Northern Illinois Gas Co., Aurora
R. M. Lundberg, Commonwealth Edison Co., Chicago
J. M. O'Donnell, The Lummus Co., Bloomfield, N. J.
A. L. Plumley, Combustion Engineering Power Systems, Windsor
J. Pope, Science Applications, Inc.

F. A. Prange, Phillips Petroleum Corp. Bartlesville
A. Schaeffer, Metals Properties Council, New York
S. J. Schneider, National Bureau of Standards (2)
J. R. Schorr, Battelle Columbus Laboratories
G. Sorel, Exxon Research and Engineering Co., Flocham Park
J. Stevenson, Rolla Metallurgy Research Center
J. Sudbury, Consolidated Coal Co., Library, Pa.
C. Whitten, Peabody Coal Co., Columbia, Tenn.